



1 Antarctic Ice Sheet grounding line discharge from 1996 through 2023

2 Benjamin J. Davison¹, Anna E. Hogg¹, Thomas Slater¹, Richard Rigby¹

3 ¹School of Earth and Environment, University of Leeds, Leeds, LS2 9JT, UK

4 *Correspondence to:* Benjamin J. Davison (b.davison@leeds.ac.uk)

5 **Abstract.** Grounding line discharge is a key component of the mass balance of the Antarctic Ice Sheet. Here we present an
6 estimate of Antarctic Ice Sheet grounding line discharge from 1996 through to last month. We calculate ice flux at up to 100
7 m resolution through 16 algorithmically-generated flux gates, which are continuous around Antarctica. We draw on a range of
8 ice velocity and thickness data to estimate grounding line discharge. For ice thickness, we use four bed topography datasets,
9 two firn models and a temporally varying ice surface. For the ice velocity, we utilise a range of publicly-available ice velocity
10 maps at resolutions ranging from 240 x 240 m to 1000 x 1000 m, as well as new, 100 x 100 m monthly velocity mosaics
11 derived from intensity-tracking of Sentinel-1 image pairs, available since October 2014. The pixel-based ice fluxes and ice
12 flux errors are integrated within all available Antarctic ice stream, ice shelf and glacier basins. Our dataset also includes the
13 contributions to discharge from changes in ice thickness due to surface lowering, time-varying firn air content and surface
14 mass change between the flux gates and grounding line. We find that Antarctic Ice Sheet grounding line discharge increased
15 from $1,990 \pm 23 \text{ Gt yr}^{-1}$ to $2,205 \pm 18 \text{ Gt yr}^{-1}$ between 1996 and 2023, much of which was due to acceleration of ice streams
16 in West Antarctica but with substantial contributions from ice streams in East Antarctica and glaciers on the Antarctic
17 Peninsula. The uncertainties in our discharge dataset primarily result from uncertain bed elevation and flux gate location,
18 which account for much of difference between our results and previous studies. It is our intention to update this discharge
19 dataset each month, subject to continued Sentinel-1 acquisitions and funding availability. The datasets are freely available at
20 <https://zenodo.org/records/10183327> (Davison et al., 2023a).

21 1 Introduction

22 The Antarctic Ice Sheet is losing mass at an accelerating rate (Diener et al., 2021; Ootosaka et al., 2023; Shepherd et al., 2019;
23 Slater et al., 2021). Much of this mass loss originates in West Antarctica, where ice streams draining into the Amundsen Sea
24 Embayment have accelerated dramatically during the satellite era (Konrad et al., 2017; Mouginot et al., 2014). As such, the
25 majority of mass loss from the Antarctic Ice Sheet is attributable to increases in grounding line discharge – the flux of ice into
26 ice shelves or directly into the Southern Ocean from the grounded Antarctic Ice Sheet (henceforth ‘discharge’). Grounding
27 line discharge is therefore a key component for quantifying the ‘health’ of the Antarctic Ice Sheet, particularly when combined
28 with surface mass balance (SMB) estimates to determine overall ice sheet mass change (Rignot et al., 2019; Sutterley et al.,
29 2014). This ‘mass budget’ or ‘input-output’ approach to measuring ice sheet mass change compliments other ice sheet mass



30 change measurements derived from altimetry measurements (Shepherd et al., 2019; Smith et al., 2020) or gravimetric
31 approaches (Diener et al., 2021; Sutterley et al., 2020; Velicogna et al., 2020). The principle benefits of the input-output method
32 are two-fold. Firstly, it permits direct partitioning of mass change between SMB and discharge, which provides insight into
33 the processes driving ice sheet mass change. Secondly, discharge is derived from ice velocity and thickness datasets, which
34 can now be generated through continuous satellite-based monitoring at relatively frequent (~monthly) intervals at the continent
35 scale. These data are available at higher spatial resolution than the other mass change measurement approaches, making the
36 input-output method particularly useful in smaller drainage basins and in mountainous terrain. Despite their utility, grounding
37 line discharge measurements for Antarctica are relatively sparse (Depoorter et al., 2013; Gardner et al., 2018; Miles et al.,
38 2022; Rignot et al., 2019) resulting in only one estimate of ice sheet mass change using the input-output method (Otosaka et
39 al., 2023; Rignot et al., 2019; Shepherd et al., 2018), which means that independent verification of ice sheet mass balance
40 using this method is lacking. Furthermore, the limited available discharge estimates feeding into those mass change
41 calculations disagree in some regions and basins (for example, the Antarctic Peninsula) such that opposing conclusions
42 regarding basin-scale mass change must be reached for those basins (Hansen et al., 2021).

43 Here, we present a new grounding line discharge dataset for the Antarctic Ice Sheet. We draw on several bed topography
44 products and velocity measurements from 1996 through to last month, and we use time-varying rates of ice surface elevation
45 change and firn air content. The velocity measurements range in spatial resolution from 1x1 km annually to 100 x 100 m every
46 month since October 2014, thereby increasing the detail and frequency of continent-wide discharge estimates over time. We
47 provide these discharge estimates integrated over every published basin definition available for Antarctica – ranging in scale
48 from the whole ice sheet down to 1 km-wide glaciers on the Antarctic Peninsula. It is our intention to update this discharge
49 dataset each month, subject to continued Sentinel-1 acquisitions and funding availability. In addition, we will endeavour to
50 provide irregular updates following the release of new bed topography datasets, grounding lines and if any bugs are identified.

51 **2 Data and Methods**

52 **2.1 Bed topography, ice surface and ice thickness**

53 We estimate grounding line discharge using multiple bed elevation datasets. Our primary estimates of bed elevation and bed
54 elevation error draw predominantly on BedMachine v2 (Morlighem, 2020; Morlighem et al., 2020), but we replace the
55 BedMachine bed and bed error with a more recent regional estimate in Princess Elizabeth Land (Cui et al., 2020) and with a
56 dedicated bed topography dataset over the Antarctic Peninsula (Huss and Farinotti, 2014), after conversion to a common geoid
57 (GL04c). We use the MATLAB tool `wgs2gl04c` to perform this conversion (Greene et al., 2019). Henceforth, we refer to this
58 merged bed topography dataset as ‘FrankenBed’ (Fig. 1). We also provide discharge estimates using the bed topography data
59 and associated error from an unmodified version of BedMachine v2 and using BedMap2 (Fretwell et al., 2013).

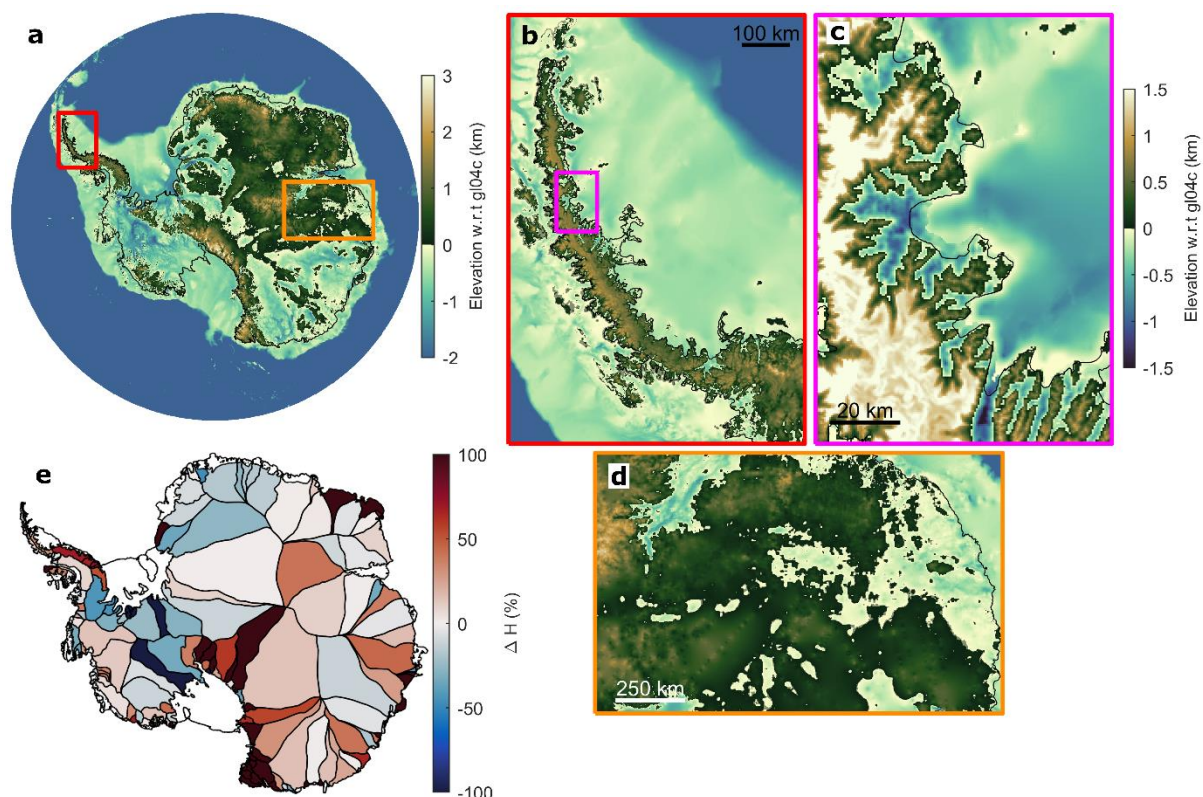


Figure 1. Antarctic Ice Sheet bed topography overview. (a) Overview of BedMachine v2. Also shown are overviews of (b) the Antarctic Peninsula (Huss and Farinotti, 2014), (c) the Larsen-B Embayment and (d) Princess Elizabeth Land (Cui et al., 2020) with FrankenBed. (e) The change in ice thickness in each MEaSUREs glacier basin in FrankenBedAdj compared to FrankenBed, where positive values indicate an increase in ice thickness. The coastline and grounding line in all figures are also shown as black lines.

60 For each of these bed products, we calculate ice thickness using the Reference Elevation Model of Antarctica (REMA) Digital
61 Elevation Model (DEM), posted at 200x200 m and timestamped to 9th May 2015 (Howat et al., 2019). Before calculating ice
62 thickness, we reference the REMA DEM elevations to the GL04c geoid and remove the climatological mean (1979–2008) firn
63 air content (Veldhuijsen, Sanne et al., 2022) (Section 2.4). Henceforth, we refer to this firn-corrected ice surface as our
64 reference ice surface, which we assume has a spatially uniform 1 m error (Howat et al., 2019). For the thickness grid calculated
65 using FrankenBed, we fill exterior gaps through extrapolation along ice flowlines using the same method applied to the
66 reference velocity map described in Section 2.3. The purpose of the extrapolation is to ensure that ice thickness estimates are
67 available at each flux gate pixel (Section 2.4). We chose to extrapolate along flowlines rather than using a more conventional
68 nearest-neighbour interpolation because the latter can lead to erroneous or poorly-targeted sampling near shear margins.



69 Even though we draw on the best available bed topography and ice surface datasets to construct FrankenBed, some ice remains
70 unrealistically thin given the observed ice flow speeds and the resulting discharge is lower than that implied by the observed
71 rates of surface elevation change and surface mass balance (Figs. A1 & A2). We therefore generate a final bed elevation
72 estimate at each of our flux gates (Section 2.4) for which we adjust the bed elevation such that the average 1996-2014 discharge
73 across each flux gate matches that required to reproduce observed basin-integrated rates of elevation change over the same
74 time period, after accounting for surface mass balance anomalies obtained from three regional climate models. This method is
75 described further in Appendix A and we refer to the resulting dataset as ‘FrankenBedAdj’ (Fig. A2). In summary, we use four
76 ice thickness estimates derived from a reference ice surface and four bed elevation datasets (Fig. 1) - BedMap2, BedMachine
77 v2, FrankenBed and FrankenBedAdj.

78 To generate an ice thickness time-series from each of these baseline thickness estimates, we modify the REMA DEM using
79 observed changes in ice surface elevation from 1992 to 2023 (Fig. A1) derived from satellite radar altimetry following the
80 methods of (Shepherd et al., 2019). Because satellite altimeter time series do not fully sample the ice sheet margins at monthly
81 intervals, either due to their orbit patterns or occasional failure in tracking challenging terrain, we estimate monthly time series
82 of ice surface elevation change by fitting time-dependent quadratic polynomials (Fig. A1) to the observed surface elevation
83 changes posted on a 5x5 km grid at quarterly intervals, which we linearly interpolate to our gate pixels and evaluate at each
84 velocity epoch (Section 2.3). We apply these modelled time-series of elevation change to each reference ice thickness estimate
85 to form time-series of ice thickness at each gate pixel. We quantify the errors in the elevation change by calculating upper and
86 lower bounds to the quadratic fit from the 95 % confidence interval on each of the model coefficients (Section 2.7.3). South
87 of 81.5°, where elevation change measurements are only available since the launch of CryoSat-2 in 2010, we assume static ice
88 thickness rather than extrapolate the historical thinning rates from those observed between 2010 and 2023. Given that the flux
89 gate pixels south of 81.5° only contribute 7 % to the pan-Antarctic discharge and that the applied thickness changes elsewhere
90 around the continent only modify the total discharge by 0.6 %, this choice has little impact on our pan-Antarctic discharge
91 estimate. We then account for temporal variations in firn air content by adjusting the climatological firn air content correction
92 in each flux gate pixel using time-series of firn air content from two firn models (Section 2.2) at each velocity epoch. For
93 discharge estimates after the last available output from each firn model, we use the monthly firn air content climatology (1979-
94 2008), in order to capture seasonal changes in firn air content. For discharge estimates after January 2023, when our thickness
95 change observations end, we continue to use the quadratic fit. We also assume no changes in bed elevation due to erosion of
96 the substrate or changes in ice thickness due to changes in subglacial melt rates, both of which are expected to be negligible.

97 **2.2 Firn air content**

98 We use two firn models (Fig. 2) to remove firn air content from our ice thickness estimates, to determine the ice equivalent
99 thickness at each flux gate and to permit the use of a single ice density value in the discharge calculation (Section 2.7). These
100 are the Institute for Marine and Atmospheric Research Utrecht Firn Densification Model (IMAU FDM) (Veldhuijsen, Sanne
101 et al., 2022) and the Goddard Space Flight Center FDM (GSFC-FDMv1.2), which draws on the Community Firn Model

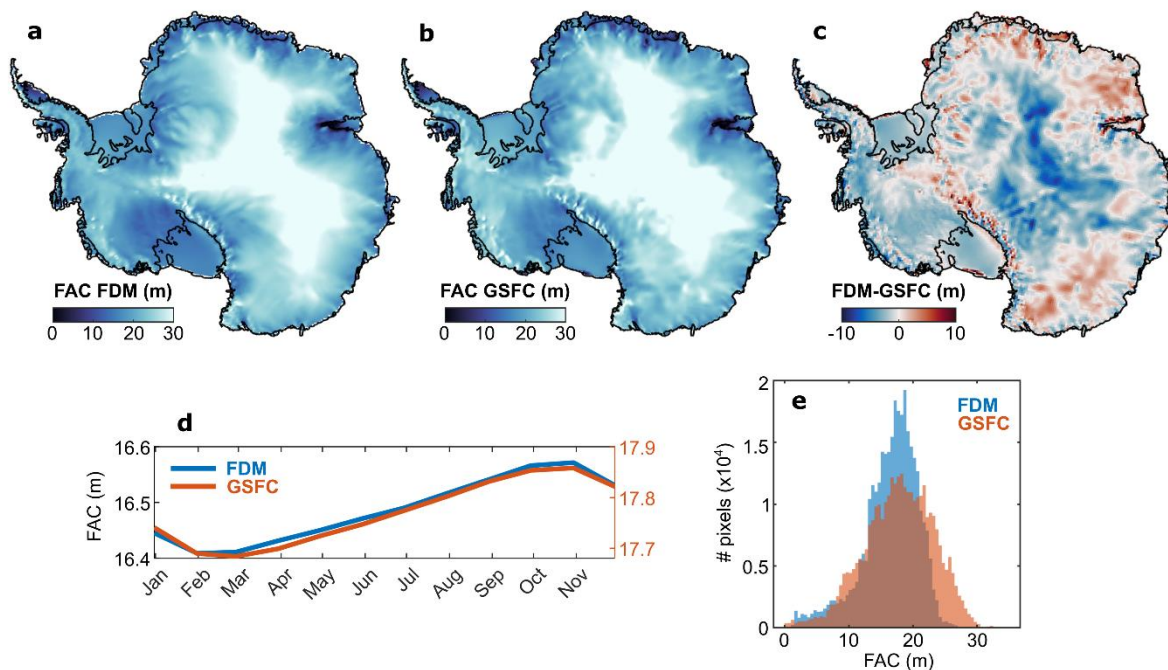


Figure 2. Overview of firn air content models. Overviews of (a) the IMAU FDM, (b) the GSFC-FDMv1.2 and (c) the difference between the two models. (d) The climatological seasonal cycle of firn air content (FAC) in each firn model. Note that in panel (d) the IMAU FDM and the GSFC-FDMv1.2 are plotted on separate y-axes to facilitate comparison of their seasonal variability; their units are the same. (e) The frequency distribution of FAC at every flux gate pixel in each model.

102 framework and is forced by the Modern-ERA Retrospective analysis for Research and Applications, Version 2 (MERRA-2)
103 climate forcing (Medley et al., 2022b, 2022a). The resolution of the IMAU FDM is 27x27 km and the GSFC-FDMv1.2 is
104 12.5x12.5 km. Both models provide daily firn air content for all of Antarctica and span the periods January 1979 to December
105 2021 for the IMAU FDM and January 1980 to July 2022 for GSFC-FDMv1.2. We use both solutions independently and
106 provide a discharge estimate using each.

107 2.3 Ice velocity

108 We generate a reference velocity dataset by combining two velocity products. First, we use a 100 x 100 m multi-year velocity
109 mosaic derived from feature tracking of Sentinel-1 imagery between January 2017 and September 2021 (Davison et al., 2023b).
110 Sentinel-1 imagery are only continuously acquired around the Antarctic Ice Sheet margin, with sparser measurements further
111 inland acquired in 2016. To fill the pole hole, we use the 450x450 m MEASUREs reference velocity product (Rignot et al.,
112 2017), which is linearly interpolated to the grid of the Sentinel-1 product. We fill interior gaps in this mosaic using the regionfill



113 algorithm in MATLAB, which smoothly interpolates inward from the known pixel values on the outer boundary of each empty
114 region by computing the discrete Laplacian over each region and solving the Dirichlet boundary value problem. This interior
115 gap-filling has no bearing on our discharge estimate, but it allows for easier filling of external gaps. We then fill exterior gaps
116 through extrapolation along flowlines following the method of Greene et al. (2022), where the observed velocity is multiplied
117 by the observed thickness mosaic (described in Section 2.1), before extrapolating along the hypothetical direction of flow and
118 inpainting between flowlines. We multiply the ice velocity by the reference ice thickness before extrapolating and inpainting,
119 so as to give appropriate weight to flow directions of thicker ice that contribute more to ice flux. As with the reference thickness
120 map, we choose to extrapolate along flowlines to avoid erroneous sampling of ice velocity, especially near shear margins. This
121 produces a gapless ice velocity map of Antarctica (Fig. 3), broadly representing the average velocity of the ice sheet from 2015
122 to 2021. We emphasise that the purpose of the gap filling is only to ensure that a velocity estimate is available at every flux
123 gate pixel. As such, the velocity in the ice sheet interior and the extrapolated velocity seaward of the flux gates in this reference
124 map have no bearing on our discharge estimate.

125 For our time-series product, we compile multiple velocity sources:

- 126 1. The 1 x 1 km MEaSURES annual velocity mosaics (Mouginot et al., 2017b, 2017a) for the year 2000 and from 2005
127 to 2016
- 128 2. Monthly 100 x 100 m velocity mosaics derived from intensity tracking of Sentinel-1 image pairs (described in
129 Appendix B), available from October 2014 to last month (Davison et al., 2023c).
- 130 3. In the Amundsen Sea Embayment in 1996, we also use a combination of 450 x 450 m MEaSURES InSAR-based
131 velocities derived from 1-day repeat ERS-1 imagery (Rignot et al., 2014), which covers the region spanning Cosgrove
132 to Kohler Glacier, and 200 x 200 m velocities from ERS-1 offset tracking over the Getz basin
133 (<https://cryoportals.enveo.at/data/>). The latter have been filled using an optimisation procedure supported by the
134 BISICLES ice sheet model (Selley et al., 2021).
- 135 4. The 240 x 240 m ITS_LIVE annual mosaics (Gardner et al., 2019) during 1996-2005.
- 136 5. Three 450 x 450 m MEaSURES multi-year velocity mosaics, which incorporate velocity estimates in the periods
137 1995-2001, 2007-2009 and 2014-2017 (Rignot et al., 2022).
- 138 6. In the Amundsen Sea Embayment, gap-filled 240 x 240 m ITS_LIVE annual mosaics, from 1996 to 2018 (Gardner,
139 2023; Paolo et al., 2023)
- 140 7. Over Pine Island Glacier, 500 x 500 m mosaics of ice velocity derived from speckle-tracking of TerraSAR-X and
141 TanDEM-X imagery, averaged over 2 to 5 month periods from 2009 to 2015 (Joughin et al., 2021).

142 Each of these velocity products spans a time period; following Mankoff et al. (2019, 2020), we treat each product as an
143 instantaneous measurement with the timestamp given by the central date in the estimate.

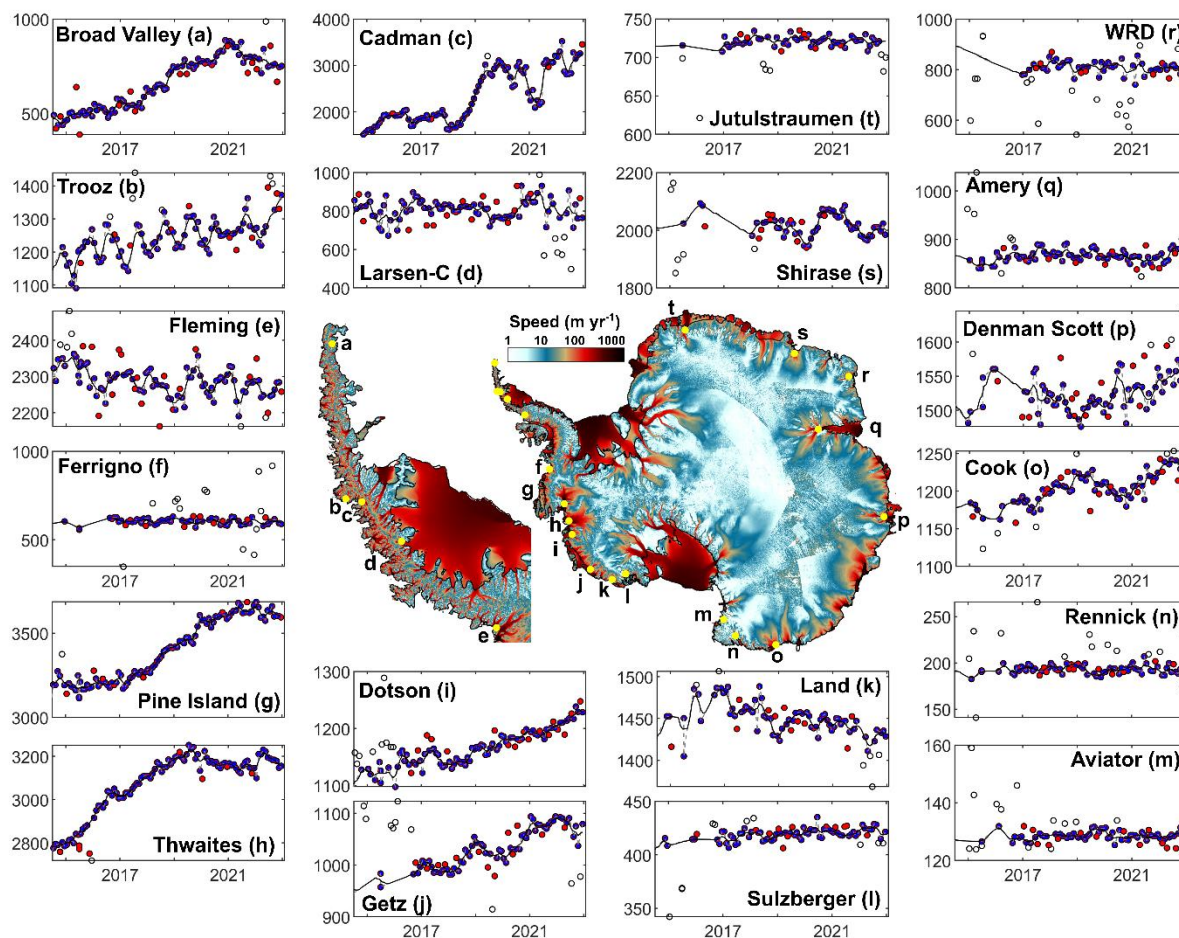


Figure 3. Reference ice velocity map and time-series outlier removal. The central plot shows the reference ice velocity map (with extrapolated velocities masked to aid visualisation). Panels (a) to (t) show example time-series of cross-gate velocity (in m yr^{-1}) extracted from single flux gate pixels. The black dots show points removed by the global outlier filters, and the red dots show points removed by the local outlier filters are shown. The unsmoothed filled time-series is shown as a grey-dashed line and the smoothed time-series is shown as a black line. WRD is Wilma Robert Downer.

144 From these data, we generate discharge-ready, gapless velocity time-series at each gate pixel as follows. We linearly interpolate
 145 the easting and northing velocities, and their respective errors, from each product to each flux gate pixel. There are consistent
 146 differences between velocity data sources that we assume are related to dataset resolution – the higher resolution datasets such
 147 as the 100×100 m Sentinel-1 mosaics and the 240×240 ITS_LIVE mosaics typically provide higher velocities than the
 148 coarser datasets, especially on narrow outlet glaciers. Treating each gate pixel as a time-series, we align each data source based



149 on a robust linear fit through their overlapping time-periods, and apply the difference between the means of each fit as a scalar
150 shift to the coarser velocity datasets. This shift increases our pan-Antarctic discharge estimate by 89 Gt yr^{-1} compared to the
151 case where we align the higher resolution datasets down to the coarser datasets.

152 Treating each flux gate pixel as a time-series, we remove outliers in two stages. Firstly, we remove global time-series outliers
153 after detrending using two passes of a scaled median absolute deviation filter with thresholds of five then two. This global
154 filter is only applied to time-series with more than 30 % of non-nan measurements. Secondly, we remove local outliers using
155 two passes of a moving median filter with a threshold of two median absolute deviations and window sizes of four months
156 then three months. We fill gaps in each of our flux gate velocity time-series in three stages. Firstly, we linearly interpolate
157 across short temporal gaps (two months or less). Secondly, we linearly interpolate across short spatial gaps (300 metres or
158 less). Thirdly, we fill remaining temporal gaps using linear interpolation, again back- and forward-filling at the ends of each
159 time-series. For gate pixels with no data at any time and more than 300 m from neighbouring finite pixels (after outlier
160 removal), we use our reference ice velocity estimate which has no gaps by definition. After infilling, we smooth each pixel-
161 based time-series with two passes of a moving mean (or boxcar) filter, with window sizes of three months then four months.
162 Where we have removed outliers then infilled the time-series, we set the easting and northing error to be $|10 \text{ \%}|$ of the
163 interpolated and smoothed easting and northing velocity components, respectively, at the gate pixel and velocity epoch in
164 question. As in previous studies (Mankoff et al., 2019, 2020; Mougnot et al., 2014), we assume the depth-averaged velocity
165 is the same as the measured surface velocity. Examples of this outlier removal and infilling are shown in Fig. 3.

166 **2.4 Flux gates**

167 We algorithmically generate 16 flux gates close to the Antarctic Ice Sheet grounding line (Fig. 4). Each flux gate is continuous
168 around the Antarctic Ice Sheet and Wilkins Island; other Antarctic islands are not included in this analysis. The seaward
169 grounding line is placed 3-years of ice flow upstream of the MEaSURES grounding line (Mougnot et al., 2017c). The ice
170 velocity for this migration is taken from the reference velocity dataset (described in Section 2.3) and the migration is performed
171 in increments of 0.1 years to account for variations in ice velocity along the migration path. Gate pixels are spaced every 100
172 m for ice flowing faster than 100 m yr^{-1} and 200 m for slower ice, defined on a Polar Stereographic grid (EPSG 3031) and
173 accounting for distance distortions introduced by that projection. 15 additional gates are generated at 200 m increments further
174 upstream of the first gate, such that the most upstream gate is 3 km upstream of the first gate. We provide discharge and error
175 estimates for each of these flux gates and for the mean of all of the gates, weighted by the reciprocal of the error at each gate.

176 **2.5 Thickness change between flux gates and grounding line**

177 Ice thickness changes can occur between the gate and the grounding line due to surface processes and due to subglacial melting.
178 Here, we estimate thickness changes due to surface processes only. We estimate this thickness change using the climatological
179 (1979-2008) surface mass balance from three regional climate models: RACMO2.3p2 (van Wessem et al., 2018), MAR

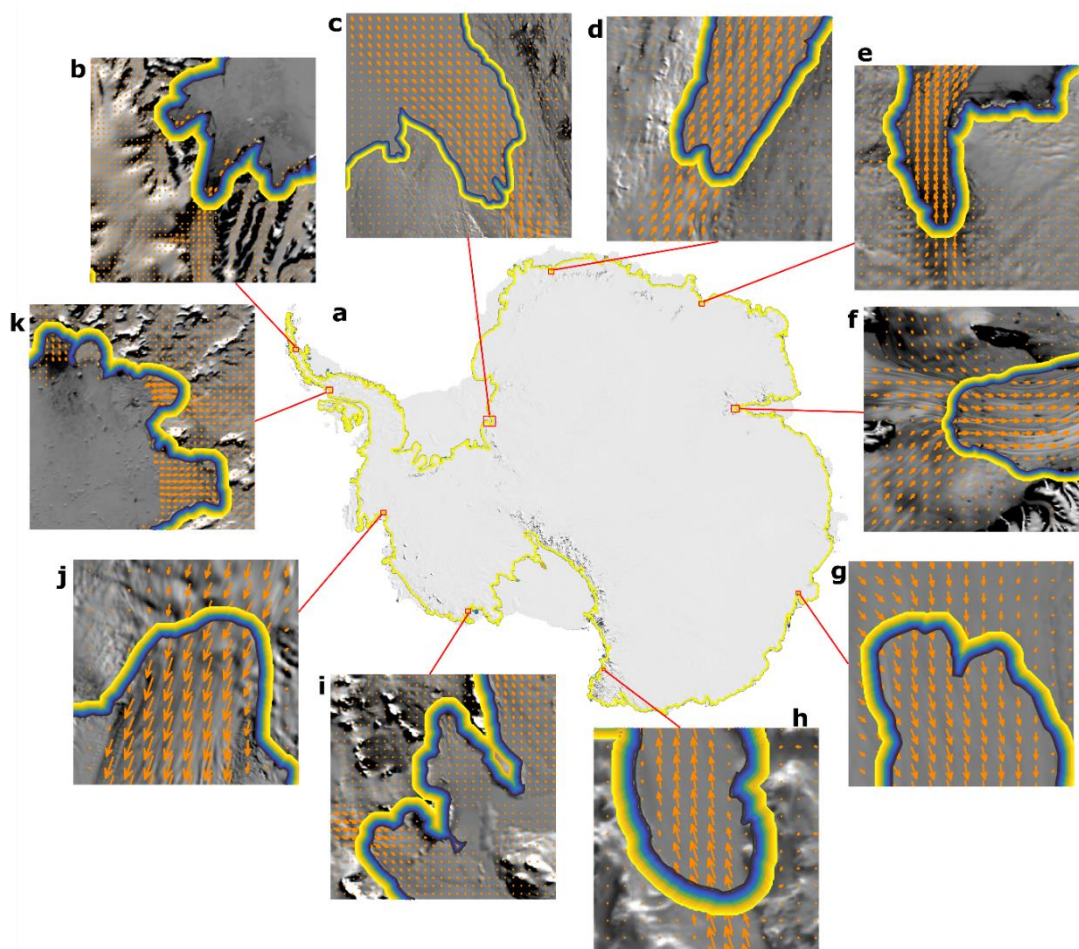


Figure 4. Flux gate overview. (a) Overview of Antarctica with flux gates plotted, where yellow lines represent the most inland gate and the blue lines represent the most seaward flux gate. Panels (b) to (k) show zoomed in examples of the 16 flux gates in small regions around Antarctica, with ice velocity vectors overlain (orange arrows). The background image is the MODIS Mosaic of Antarctica (Haran et al., 2018).

180 (Agosta et al., 2019; Kittel et al., 2018) and HIRHAM5 (Hansen et al., 2021). For each gate pixel where ice flow is greater
181 than 100 m yr^{-1} , we calculate the number of years of ice flow between each flux gate pixel and the MEASUREs grounding line
182 (Mouginot et al., 2017c), to convert this rate of thickness change to a total thickness change. We use this static thickness
183 correction at each velocity epoch. We do not perform this correction for ice flowing slower than 100 m yr^{-1} , so as to avoid
184 unrealistic modifications to the initial ice thickness.



185 2.6 Drainage basins

186 We provide a discharge estimate for all available Antarctic Ice Sheet basins (Fig. 5). This includes the MEaSURES regional
187 basins and MEaSURES glacier basins (Mouginot et al., 2017c), Zwally basins (Zwally et al., 2012), ice shelf basins (Davison
188 et al., 2023b), and Antarctic Peninsula basins (Cook et al., 2014). In total, there are 966 basins used in this study. For each
189 basin, we provide the discharge through each of the 16 flux gates and the average of all flux gates (weighted by the reciprocal
190 of their respective errors) along with their errors. These metrics are provided using each of the four bed topography estimates
191 and with two firm models. In total, therefore, we provide 136 discharge time-series for each basin. In addition, we provide the
192 impact of the three ice thickness corrections – (1) IMAU FDM firm air content; (2) downstream surface mass balance, and; (3)
193 ice surface elevation changes - on each basin-integrated discharge estimate for each flux gate.

194 2.7 Grounding line discharge

195 2.7.1 Balance discharge

196 We define the balance discharge as the discharge required to maintain the mass of a given ice sheet basin on ‘long’ time-scales
197 (decades). In order to maintain the mass of a basin, the hypothetical balance discharge would therefore need to equal the basin-
198 integrated SMB input on average. Accordingly, we estimate the balance discharge of each basin by integrating the 1979-2008
199 SMB from the mean of three regional climate three-models (RACMO2.3p2, MAR and HIRHAM5) within each of the above
200 basins. We estimate the balance discharge error in each basin as the standard deviation of 10 realizations of 20-year
201 climatologies from 1979 to 2008 (i.e. 1979-1999, 1980-2000, etc.). Note that only RACMO2.3p2 is available in 1979.

202 2.7.2 Discharge

203 We estimate grounding line discharge, D , across each flux gate pixel as:

$$204 \quad D = VHw\rho, \quad (4)$$

205 where V is the gate-normal ice velocity, H is the ice equivalent thickness, w is the pixel width and ρ is ice density (917 kg m^{-3}).
206

207 The gate-normal ice velocity is given by:

$$208 \quad V = \sin(\theta)V_x - \cos(\theta)V_y, \quad (5)$$

209 where V_x and V_y are the easting and northing components of the horizontal ice velocity, as defined by the South Polar
210 Stereographic grid (EPSG3031), respectively, and θ is the angle of the flux gate relative to the same grid. To calculate the total

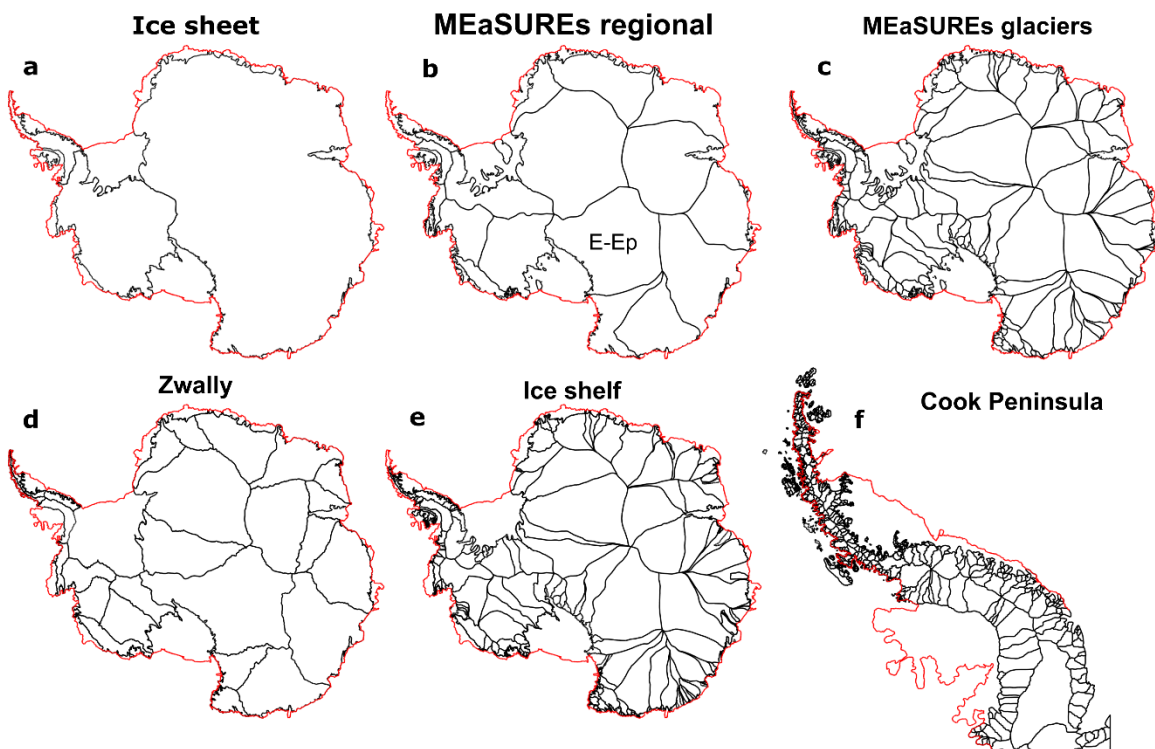


Figure 5. Overview of Antarctic Ice Sheet drainage basins. (a) Main ice sheet basins – East Antarctica, West Antarctica and the Antarctic Peninsula. Also shown are smaller drainage basin definitions, including (b) the MEaSUREs regional basins, (c) the MEaSUREs glacier basins, (d) the Zwally basins, (e) ice shelf basins and (f) the Peninsula glacier basins. The coastline is shown in red.

211 discharge from each basin at each velocity measurement epoch, we simply sum the discharge through each flux gate pixel
212 contained within the basin.

213 2.7.3 Discharge error

214 We define our discharge error in each flux gate pixel, D_σ , as:

$$215 \quad D_\sigma = \sqrt{V_\sigma^2 + H_\sigma^2}, \quad (6)$$

216 where V_σ is the velocity-induced discharge error and H_σ is the thickness-induced discharge error. Both sources of discharge
217 error are timestamped and calculated at each flux gate pixel. We calculate the velocity-induced discharge error as:

$$218 \quad V_\sigma = ((D_{ref} - D_{Vmin}) + (D_{Vmax} - D_{ref}))/2, \quad (7)$$



219 where D_{ref} is the reference discharge estimate at each epoch. D_{Vmin} and D_{Vmax} are the discharges derived using lower and
 220 upper bounds on the gate-normal velocity, V , given by the velocity error, V_σ . The minimum and maximum gate-normal
 221 velocities, V_{min} and V_{max} , are determined from the error in the gate-normal velocity, which in turn is calculated from the errors
 222 in the easting and northing velocity components:

$$223 \quad V_{xmax} = \sin(\theta)V_{xmax} - \cos(\theta)V_y,$$

$$224 \quad V_{xmin} = \sin(\theta)V_{xmin} - \cos(\theta)V_y,$$

$$225 \quad V_{ymax} = \sin(\theta)V_x - \cos(\theta)V_{ymax},$$

$$226 \quad V_{ymin} = \sin(\theta)V_x - \cos(\theta)V_{ymin},$$

$$227 \quad V_\sigma = \sqrt{(V - V_{xmax})^2 + (V - V_{xmin})^2 + (V - V_{ymax})^2 + (V - V_{ymin})^2},$$

$$228 \quad V_{min} = V - V_\sigma,$$

$$229 \quad V_{max} = V + V_\sigma, \quad (8)$$

230 Similarly, we calculate the thickness-induced discharge error as:

$$231 \quad D_\sigma = ((D_{ref} - D_{Hmin}) + (D_{Hmax} - D_{ref}))/2, \quad (9)$$

232 where D_{Hmin} and D_{Hmax} are the discharges derived using lower and upper bounds on the local ice thickness given by the
 233 thickness error. The thickness error, H_σ , is calculated as:

$$234 \quad H_\sigma = \sqrt{(B_\sigma + 1)^2 + \Delta H_\sigma^2}, \quad (10)$$

235 where B_σ is the bed elevation error taken from the respective bed elevation products, to which we add 1 meter of ice surface
 236 elevation error (Howat et al., 2019). ΔH_σ is the error in the applied surface elevation change timeseries, which we calculate as:

$$237 \quad \Delta H_{max} = t(a + a_\sigma)^2 + t(b + b_\sigma) + (c + c_\sigma),$$

$$238 \quad \Delta H_{min} = t(a - a_\sigma)^2 + t(b - b_\sigma) + (c - c_\sigma),$$

$$239 \quad \Delta H_\sigma = \left(\frac{\lambda_1}{\lambda_0}\right) \left(\frac{(\Delta H_{max} - \Delta H) + (\Delta H - \Delta H_{min})}{2}\right). \quad (11)$$

240 Here, a , b and c are the quadratic, linear and intercept coefficients of the quadratic fit to the ice surface elevation change data.
 241 a_σ , b_σ and c_σ provide the bounds on the 95 % confidence interval for each coefficient. λ_0 and λ_1 are the sampling frequency of
 242 the fit (monthly) and the original observations (every 140 days) on which the fit is based, which together provide a scaling



243 factor that prevents the uncertainty in ΔH scaling with the observational frequency. The total pixel-based errors are typically
244 10 to 30 % of the pixel-based discharge estimates.

245 We calculate the basin-integrated error in two ways. Firstly, we use the root-sum-square of the discharge error at each flux
246 gate pixel contained within the basin. This root-sum-square approach assumes the errors of neighbouring flux gate pixels are
247 independent and reduces the basin-integrated errors to around 1 % of the basin-integrated discharge. As such, it represents a
248 lower bound on the error in the discharge dataset. Secondly, we also provide the 95 % confidence interval of the gate-mean
249 discharge based on the standard error of the discharge estimates through each of the 16 flux gates. The latter approach provides
250 a measure of the uncertainty in the discharge estimate associated with the gate location, which in turn reflects the errors in the
251 underlying ice velocity and ice thickness datasets. In the following, all plots and statistics use this confidence interval metric
252 of discharge uncertainty.

253 **3 Results**

254 **3.1 Grounding line discharge**

255 We provide grounding line discharge estimates through 16 flux gates using four bed topography products and two firm models
256 for 966 drainage basins. In the following, we primarily present values from the mean of all flux gates (weighted by the
257 reciprocal of their errors) using our favoured bed topography dataset (FrankenBed) and the IMAU FDM. We also present
258 comparisons across gates, bed topography datasets and firm models in turn.

259 Our primary discharge dataset (Fig. 6) gives a total Antarctic grounding line discharge of $1,990 \pm 23$ Gt yr⁻¹ in July 1996,
260 rising to $2,205 \pm 18$ Gt yr⁻¹ in September 2023. On average, Antarctic discharge has increased at a rate of 6.5 Gt yr⁻² or 0.3 %
261 yr⁻² over the study period from 1996. Our dataset shows that Antarctic grounding line discharge has fluctuated slightly through
262 our time period. Discharge increased steadily from 1998 to 2012 and since 2018. These periods of rising discharge were
263 interrupted by a slight decline in discharge from 2012 to 2014 and relatively steady discharge from 2014 to 2018.

264 Our dataset also provides grounding line discharge measurements for distinct Antarctic regions (Fig. 6). Grounding line
265 discharge from West Antarctica increased from 790 ± 8 Gt yr⁻¹ in July 1996 to 943 ± 7 Gt yr⁻¹ in September 2023, with a trend
266 of 5.8 Gt yr⁻² or 0.6 % yr⁻² and following a similar pattern of temporal variability described above. West Antarctica therefore
267 currently accounts for approximately 43 % of all Antarctic grounding line discharge and 70 % of the total Antarctic increase
268 in discharge from 1996 to 2023. Discharge from East Antarctica has also increased from 945 ± 13 Gt yr⁻¹ in 1996 to 977 ± 9
269 Gt yr⁻¹ in June 2023, with a statistically significant trend of 1.3 Gt yr⁻². However, East Antarctic discharge is the most uncertain
270 of any region and fluctuated on approximately 10-year time-scales with an amplitude of approximately 20 Gt yr⁻¹. This relative
271 large uncertainty and temporal variability means that East Antarctic grounding line discharge in 2015 was not significantly
272 different from that in 2002, and may explain previous reports of unchanging East Antarctic grounding line discharge that were
273 based on comparisons between two epochs (Gardner et al., 2018). Grounding line discharge from the Antarctica Peninsula was

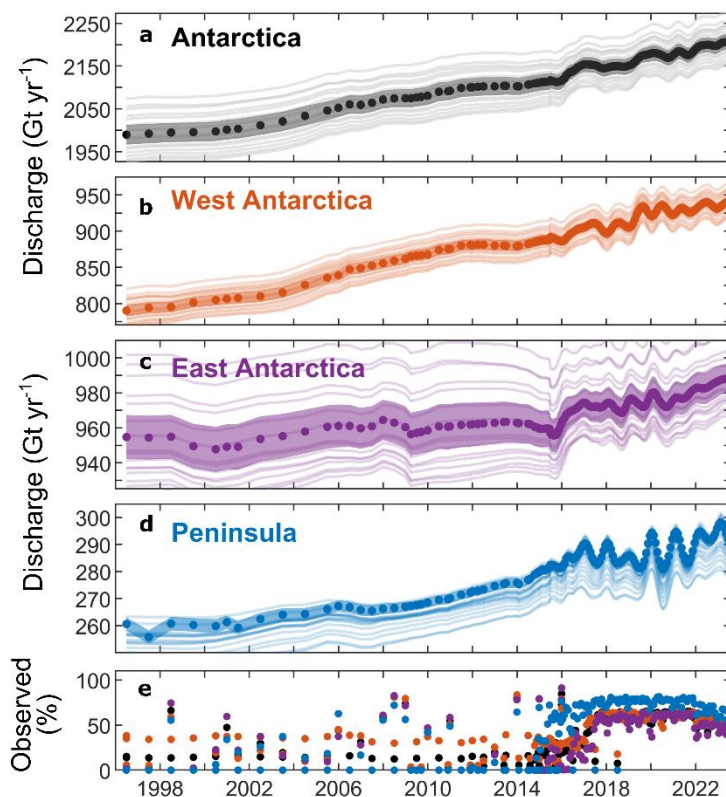


Figure 6. Antarctic Ice Sheet grounding line discharge. Discharge time-series for (a) Antarctica, (b) West Antarctica, (c) East Antarctica and (d) the Antarctic Peninsula. In each panel, the dots show the central discharge estimate with 95 % confidence bounds (shading) and the discharge through each individual flux gate (faint lines). (e) The proportion of discharge that is observed, as opposed to infilled, shown for the whole Antarctic Ice Sheet (black dots), West Antarctica (orange dots), East Antarctica (purple dots) and the Antarctic Peninsula (blue dots).

274 $261 \pm 2 \text{ Gt yr}^{-1}$ in 1996, increasing to $292 \pm 6 \text{ Gt yr}^{-1}$ on average during April to September 2023, with a trend of 1.4 Gt yr^{-2} or
275 $0.5 \% \text{ yr}^{-2}$. Our monthly discharge estimates since 2015 contain pronounced seasonal variations in discharge on the Antarctic
276 Peninsula as a whole and on many of its outlet glaciers, as shown by two other studies to date (Boxall et al., 2022; Wallis et
277 al., 2023). The seasonal cycles across the whole Peninsula have an amplitude of approximately $10\text{-}15 \text{ Gt yr}^{-1}$ but with
278 substantial variability between years. (Fig. 6).

279 Within the above regions, we provide discharge time-series for individual glacier, ice stream and ice shelf basins. A selection
280 of these basins, spanning discharges from less than 0.3 Gt to over 100 Gt , are shown in Fig. 7. The top five contributors to
281 Antarctic-wide grounding line discharge, on average since 2016, are Pine Island Glacier ($144 \pm 9 \text{ Gt yr}^{-1}$), Thwaites Glacier

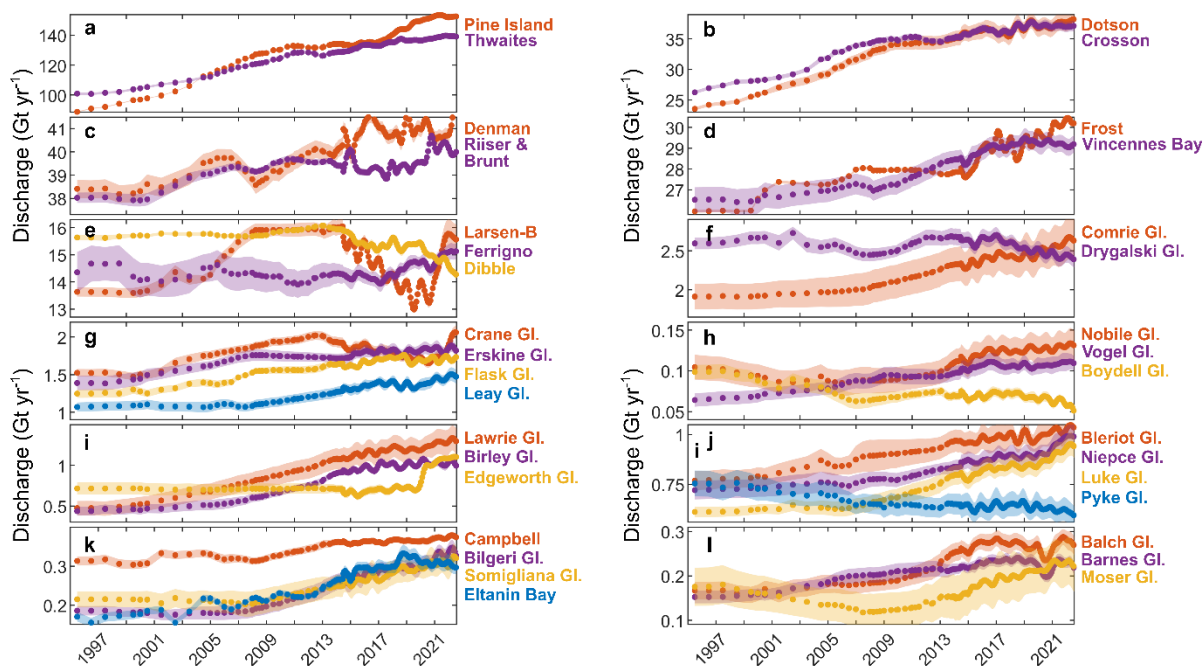


Figure 7. Basin-scale grounding line discharge examples. Grounding line discharge for selected basins from 1996 to 2023. The points show the gate-average discharge estimate and the shading shows the discharge uncertainty (95 % confidence limits). Glacier locations in Figure 8.

282 ($136 \pm 10 \text{ Gt yr}^{-1}$), Getz drainage basin ($104 \pm 4 \text{ Gt yr}^{-1}$), Totten Glacier ($85 \pm 1 \text{ Gt yr}^{-1}$) and George VI ($72 \pm 4 \text{ Gt yr}^{-1}$).
 283 Discharge from Pine Island Glacier increased from $89 \pm 0.2 \text{ Gt yr}^{-1}$ to $153 \pm 0.6 \text{ Gt yr}^{-1}$ from 1996 to September 2023, but this
 284 increase was interrupted by relatively steady discharge from 2009 to 2017 and from late-2021 to 2023 (Fig. 7a). Our dataset
 285 also includes other well-known changes in grounding line discharge around Antarctica, including increases at Thwaites
 286 Glacier, Crosson and Dotson ice shelves (Fig. 7a,b), and decreases at Drygalski Glacier particularly since 2010 (Fig. 7f) and
 287 Kamb Ice Stream (Fig. 8). Our dataset also reveals substantial changes in discharge at some glaciers and ice shelves that are
 288 less well-known, including increases in discharge from Cook Ice Shelf basin (Miles et al., 2022), Muller Ice Shelf, Denman
 289 Scott Glacier, Vincennes Bay (primarily from Vanderford Glacier), Frost Ice Shelf, Ferrigno Ice Shelf, as well as numerous
 290 glaciers on the Antarctic Peninsula (Fig. 7).

291 Fig. 8 provides an overview of 1996 to 2023 trends in grounding line discharge from individual glacier and ice stream basins
 292 around Antarctica. This overview highlights increasing grounding line discharge in much of West Antarctica, especially along
 293 the Amundsen Sea coastline, many basins in the Antarctica Peninsula and across the Indian Ocean-facing sector of Antarctica.

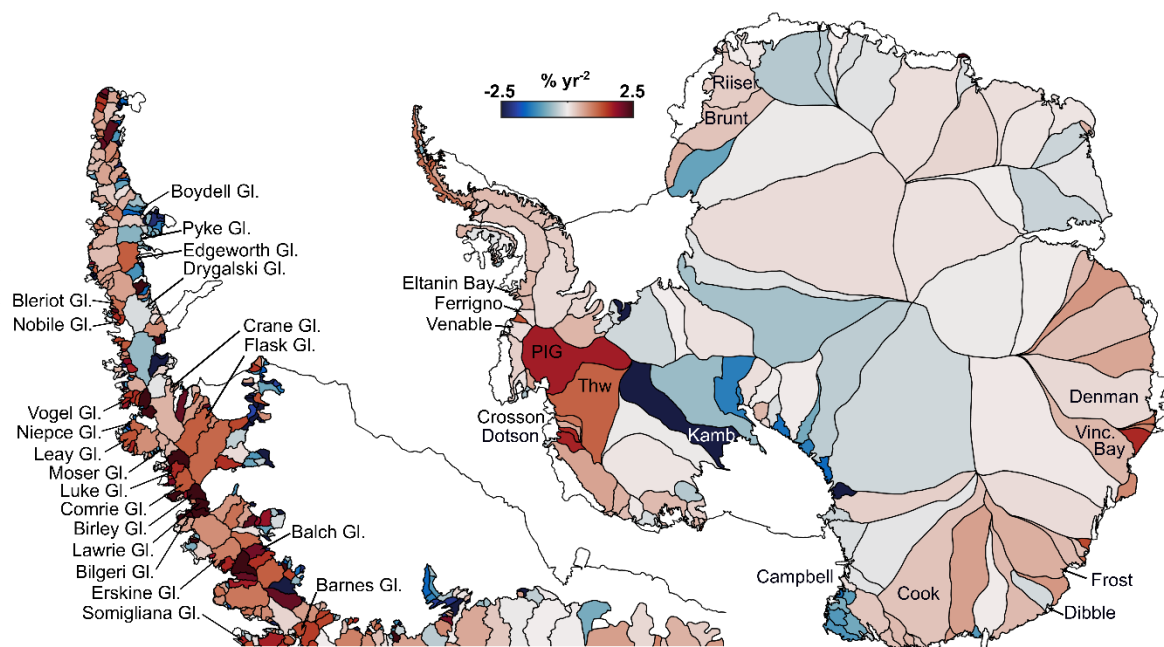


Figure 8. Basin-scale grounding line discharge trends from 1996 to 2023. Overview of grounding line discharge trends from 1996 to 2023, as a percentage of the 1996 to 2023 median discharge in each drainage basin. Basins mentioned in the main text and Figure 7 are labelled. Some basin names have been shortened for display purposes: “Vinc. Bay” is Vincennes Bay; “PIG” is Pine Island Glacier; “Thw” is Thwaites; “Riiser” is Riiser-Larsen.

294 It also highlights decreasing grounding line discharge from many glaciers and ice streams feeding the Ross Ice Shelf, from
295 glaciers draining Oates Land in East Antarctica, and from glaciers (for example, Boydell Glacier) surrounding Longing
296 Peninsula on the Antarctic Peninsula (Fig. 8). This broad spatial pattern of grounding line discharge change is consistent with,
297 but adds more detail to, changes in ice sheet surface elevation over a similar time period (Shepherd et al., 2019).

298 3.2 Effect of bed topography dataset on discharge

299 Excluding FrankenBedAdj, the choice of bed topography dataset affects the Antarctic-wide discharge estimate by 55 Gt yr⁻¹
300 on average (Fig. 9). At the continent scale, FrankenBed produces the highest discharge and BedMachine and BedMap2
301 respectively produce discharge 3.9 % and 3.4 % lower than with FrankenBed. In West Antarctica, the difference between
302 FrankenBed and BedMachine is negligible and the difference with BedMap2 is 3 %. In East Antarctica, BedMachine produces
303 0.4 % less discharge than FrankenBed, whilst BedMap2 produces 2.3 % more than FrankenBed. The bed datasets differ most
304 on the Antarctic Peninsula, where BedMachine and BedMap2 give 29 % and 26 % less discharge than FrankenBed (Fig. 9),
305 which we attribute to the overly-shallow topography and therefore implausibly thin ice given by those datasets on the

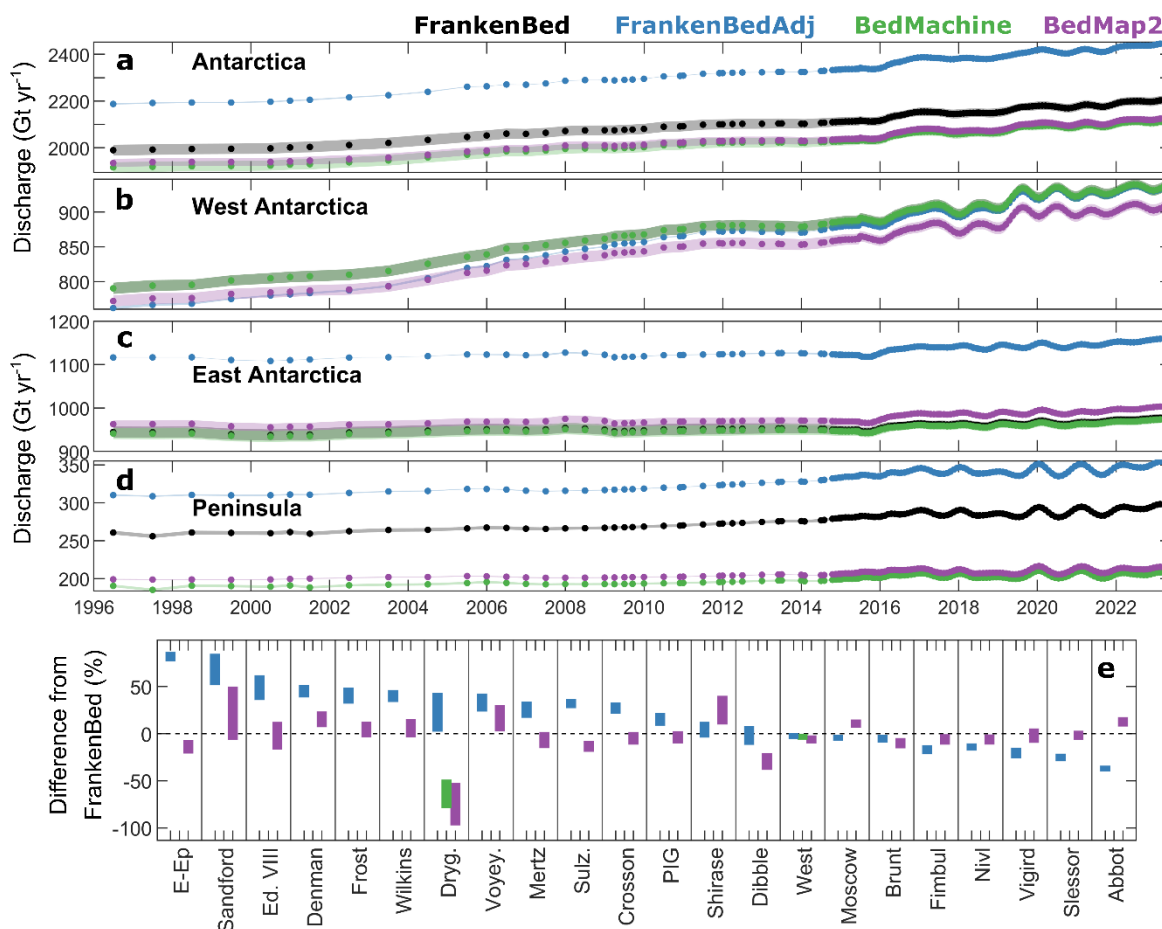


Figure 9. Impact of bed topography dataset on grounding line discharge. Grounding line discharge time-series averaged across all flux gates for (a) Antarctica, (b) West Antarctica, (c) East Antarctica and (d) the Antarctic Peninsula. Panel (e) shows the percentage difference in grounding line discharge produced using FrankenBedAdj, BedMachine and BedMap2 compared to FrankenBed, for a range of drainage basins. The vertical extent of each bar represents the potential spread in the differences between bed products owing to error in each discharge estimate. Note that FrankenBed and BedMachine are identical for all displayed basins except West. Some basins have been shortened for display purposes: “Ed. VIII” is Edward VIII, “Dryg.” is Drygalski Glacier, “Voyey.” is Voyeykov Ice Shelf and “Sulz.” is Sulzberger Ice Shelf.

306 Peninsula. Within individual MEaSURES glacier basins, BedMachine typically causes either positive or negative discharge
 307 changes of 2.5 % or less compared to FrankenBed and BedMap2 typically underestimates discharge by 2.5-7.5 % relative to
 308 FrankenBed (Fig. 9f). The impact can be much larger for some individual basins; for example, the discharge from Hektor



309 Glacier is 90 % lower using BedMachine than it is with FrankenBed and the differences are typically greater than 75 % for
310 individual glaciers on the Peninsula. The standard error of discharge across our 16 flux gates is similar between FrankenBed,
311 BedMachine and BedMap2, despite the increase in bed topographic observations and improvements in interpolation and
312 assimilation methods since BedMap2 was developed.

313 Our grounding line discharge estimate derived using FrankenBedAdj differs substantially from that using the other bed
314 products in the majority of basins, with the largest differences between FrankenBedAdj and FrankenBed are in East Antarctica
315 and the Peninsula (Fig. 9). In basin E-Ep in East Antarctica (location in Fig. 5), FrankenBedAdj produces a discharge more
316 than 80 % greater than that using FrankenBed (Fig. 9). On the Peninsula, FrankenBedAdj produces a discharge estimate almost
317 20 % greater than that derived from FrankenBed (Fig. 9). Some of the differences between FrankenBedAdj and the other bed
318 topography products will be due to unknown uncertainties in SMB modelling, particularly in Victoria Land where SMB models
319 disagree substantially (Mottram et al., 2021). Nevertheless, basins in which the discharge from FrankenBedAdj differ
320 substantially from FrankenBed (Fig. A2) could be useful areas to target future bed topographic mapping campaigns. We
321 reiterate that the derivation of FrankenBedAdj assumes that ice thickness is the only contributor to differences between mass
322 balance estimates derived from the input-output method and altimetry measurements (Appendix A), so we consider these
323 discharge differences upper bounds on that owing to uncertainties in bed topography.

324 **3.3 Effect of gate location**

325 Antarctic-wide grounding line discharge varies by 99 Gt yr^{-1} (4.5 %) on average from 1996 to 2023 between our most upstream
326 and downstream flux gates, and individual gates are generally less than 2 % different from the gate-average discharge (Fig.
327 10). The Antarctic Peninsula is the area with the largest relative differences between flux gates, where the most upstream and
328 downstream gates differ from each other by 6 %. The differences between flux gates primarily reflects the difficulty in
329 conserving mass with imperfect ice thickness, velocity and surface mass balance data, rather than algorithmic errors. Reflective
330 of this, the location of the flux gate makes a small difference for basins where the bed is well surveyed. For example, at Pine
331 Island Glacier, the maximum discharge difference between any flux gate and the gate-average is just 1.7 Gt yr^{-1} (1.3 %). Some
332 studies (Davison et al., 2023c; Gardner et al., 2018) have minimised the impact of uncertain bed topography by placing their
333 flux gates directly over bed topographic observations (primarily from radar flight lines). We opt instead to use the inverse
334 error-weighted average of all gates, which has the advantage of permitting algorithmic gate generation and will prioritise gates
335 positioned closer to bed elevation observations since the error in the bed products is primarily determined by the distance to
336 the nearest bed elevation observation.

337 **3.4 Effect of thickness adjustments**

338 We apply three modifications to the reference ice thickness extracted at each flux gate. These are (1) applying observed rates
339 of surface elevation change based on a quadratic fit to elevation change observations from 1992 to 2023 to obtain a time-series
340 of ice thickness at each flux gate pixel; (2) the removal of firn air content using a time-series of firn air content from two firn

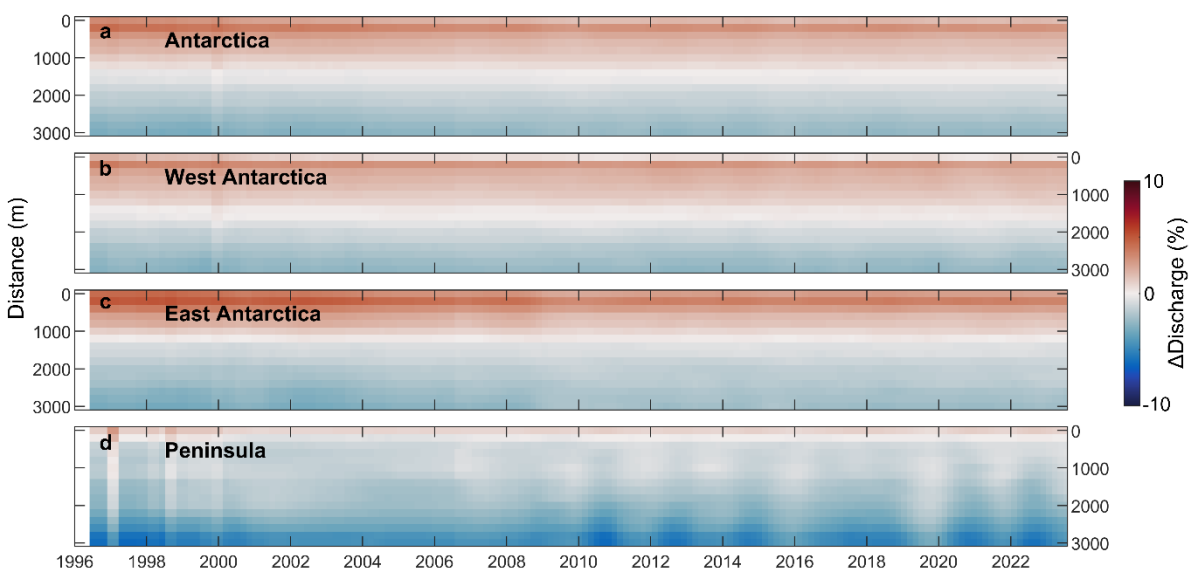


Figure 10. Impact of flux gate location on grounding line discharge. Time-series of the percentage difference in grounding line discharge from the inverse error-weighted mean discharge across all flux gates for (a) Antarctica, (b) West Antarctica, (c) East Antarctica and (d) the Antarctic Peninsula. The y-axes correspond to the distance upstream of the first flux gate.

341 models, and; (3) a correction for any changes in ice thickness that occur between the flux gate and the grounding line due to
342 surface processes. Antarctic-wide, the overall impact of these modifications is to reduce grounding line discharge by 27 Gt yr⁻¹
343 ¹ in 1996 and by 58 Gt yr⁻¹ in 2023 (Fig. 11). The majority of the reduction in discharge from these modifications is due to the
344 removal of firm air content, which reduces Antarctic grounding line discharge by 59 Gt yr⁻¹ on average, with a standard
345 deviation of 2 Gt yr⁻¹, when using the IMAU FDM. The majority of the change in the impact of these modifications from 1996
346 to 2023 is due to changes in ice surface elevation during that period, which cause an overall decrease in discharge of 26 Gt yr⁻¹
347 ¹ from 1996 to 2023 (Fig. 11). The impact of surface elevation changes on grounding line discharge is greatest in West
348 Antarctica, where thinning rates are highest (Fig. A1). The impact of firm air content removal is comparable in East and West
349 Antarctica (approximately 22 Gt yr⁻¹ or 2 % discharge reductions each, on average) and is greatest in relative terms on the
350 Peninsula (14 Gt yr⁻¹ or 5 %). The effect of gate-to-grounding line thickness changes from SMB is to increase Antarctic
351 grounding line discharge by 14-17 Gt yr⁻¹ (Fig. 11).

352 The choice of firm densification model has a negligible (0.4 %) impact on Antarctic-wide grounding line discharge (Fig. 12),
353 regardless of which flux gate is used. The IMAU-FDM produces slightly higher discharge values than the GSFC-FDMv1.2.
354 The differences between the firm models are generally greatest (~1 % discharge equivalent) on the Peninsula, which we

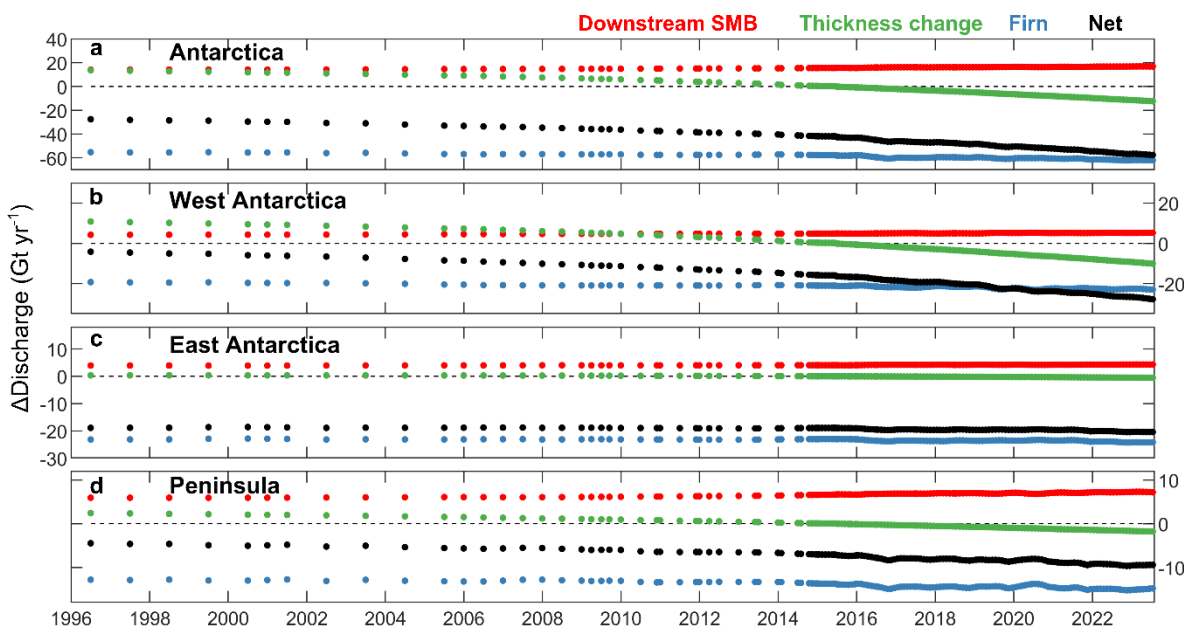


Figure 11. Timeseries of ice thickness corrections. The impact of our three ice thickness adjustments, which include SMB changes downstream of the flux gate (red dots), altimetry-derived thickness change (green dots) and removal of firn air content (blue dots) (described in text) on the derived grounding line discharge from (a) Antarctica, (b) West Antarctica, (c) East Antarctica and (d) the Antarctic Peninsula. The sum of the three corrections is also shown (black dots). A negative change in discharge equates to an ice thinning. Note that surface elevation changes are applied to our reference Antarctic Ice Sheet surface, which is timestamped to 9th May 2015.

355 interpret to be primarily due the ability of each model to resolve the impact of steep topography on surface processes, owing
356 to their different spatial resolutions (12.5x12.5 km for the GSFC-FDMv1.2 and 27x27 km for the IMAU FDM). In some
357 basins, the choice of firn model makes an appreciable difference – for example, at Moser Glacier, the IMAU-FDM decreases
358 grounding line discharge by 4 % relative to the GSFC-FDMv1.2 on average. Basins with large relative differences are generally
359 very small – with widths much less than the resolution of either firn model - so contribute little to total Antarctic discharge
360 and require extraction from a single firn model pixel that will in many cases not resolve the glacier geometry. Overall then,
361 the use of a firn model has a large enough impact on grounding line discharge to be relevant to glacier mass balance, but the
362 choice of firn model seems to have little impact on Antarctic discharge, at least for the two firn models examined here.
363

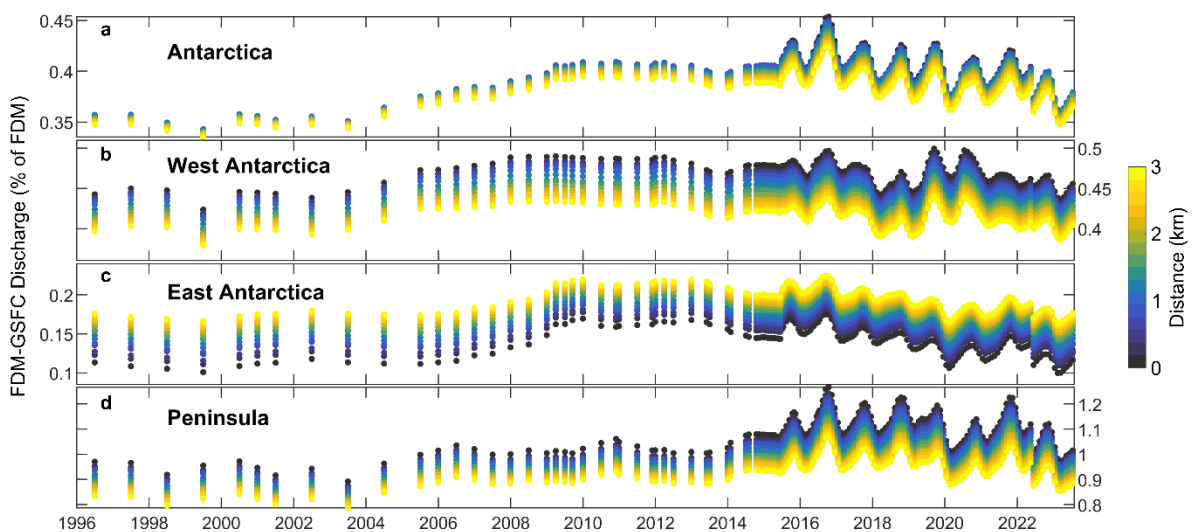


Figure 12. Impact of firm model choice on Antarctic grounding line discharge. Time-series of the difference in grounding line discharge when using the IMAU FDM compared to the GSFC-FDMv1.2 from (a) Antarctica, (b) West Antarctica, (c) East Antarctica and (d) the Antarctica Peninsula. Point are coloured according to their distance in kilometres from the most downstream flux gate (blue) compared to the most inland flux gate (yellow).

364 4 Discussion

365 4.1 Comparison to previous estimates

366 Surprisingly few estimates of Antarctic grounding line discharge have been published and made freely available, so we hope
367 that the community will benefit from the release of the dataset described in this study. We focus our comparison on previous
368 estimates that encompass the majority or all of the Antarctic Ice Sheet (Depoorter et al., 2013; Gardner et al., 2018; Miles et
369 al., 2022; Rignot et al., 2019). We note that the ‘2008’ discharge estimates from Gardner et al. (2018) and Depoorter et al.
370 (2013) were estimated using a velocity mosaic (Rignot et al., 2017) compiled from images acquired during the 1996 to 2009
371 period, but the majority of those images were acquired between 2007 and 2009. To compare our discharge time-series to those
372 data, we use our average discharge from January 2007 to December 2009. Rignot et al. (2019) used a range of methods to
373 estimate grounding line discharge; we restrict our comparison to basins for which discharge was estimated using a comparable
374 method (i.e. using both measured ice velocity and ice thickness).

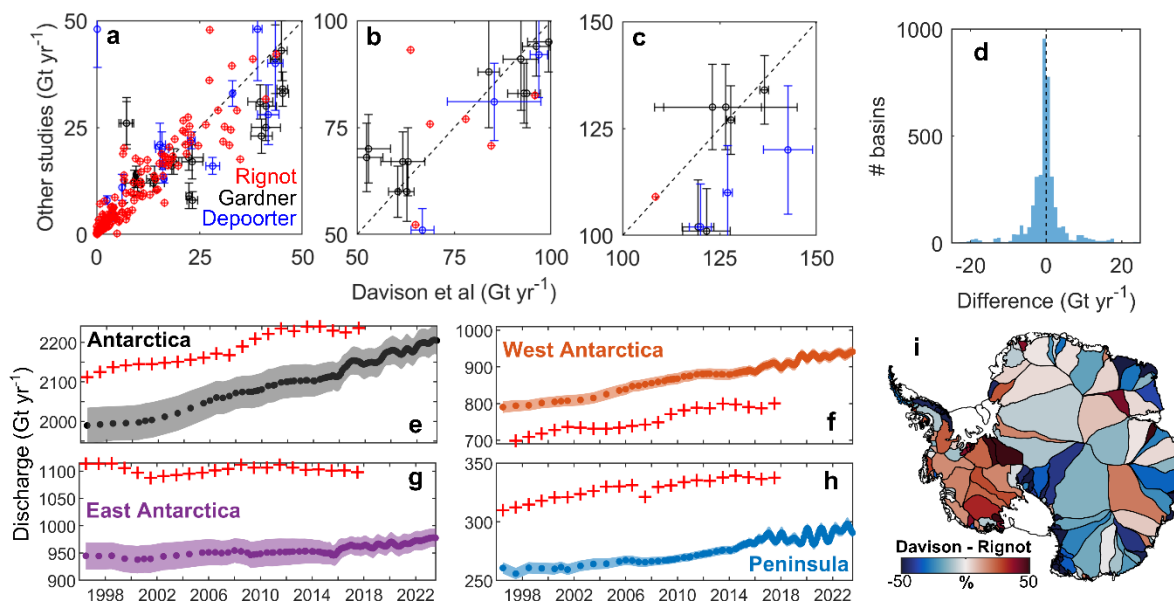


Figure 13. Comparison to existing grounding line discharge estimates. Panels (a) to (c) show comparisons with Rignot et al. (2019), Gardner et al. (2018) and Depoorter et al. (2013) for equivalent basins and during overlapping time-periods. Each point shows the discharge for a single basin, with errors provided where available. (d) Histogram of the discharge residuals from panels (a) to (c). Panels (e) to (h) show time-series of our primary discharge estimate (using FrankenBed) compared to estimates from Rignot et al. (2019) (red crosses). (i) Basin-scale comparison of discharge between this study and Rignot et al. (2019) during their overlapping time periods, as a percentage of the Rignot discharge.

375 There are substantial differences between discharge estimates for some basins and for Antarctica, East Antarctica, West
 376 Antarctica and the Antarctic Peninsula as a whole (Fig. 13). The average absolute difference between our discharge estimates
 377 and the available alternative estimates is 5 Gt yr⁻¹. In some basins, the differences are much larger. For example, Depoorter et
 378 al. (2013) estimate the discharge from Filchner-Ronne to be 69 Gt yr⁻¹ (23 %) lower than in this study, the discharge from
 379 Brunt and Riiser-Larsen to be 9 Gt (23 %) greater, the discharge from Pine Island to be 17 Gt yr⁻¹ (13 %) lower, and the
 380 discharge from Sulzberger to be 5.6 Gt (37 %) greater than in this study. Depoorter et al. (2013) use a combination of ice
 381 thickness based on the assumption of hydrostatic equilibrium and from ice penetrating radar measurements, whereas we draw
 382 on gridded bed topography products – the differences between these thickness datasets accumulate across long flux gates like
 383 that at Filchner-Ronne, Brunt, Riiser-Larsen and Sulzberger. Depoorter et al. (2013) also use different flux gate positions than
 384 used here, which could plausibly account for much of the difference in flux estimates. To illustrate, we find a 39 Gt yr⁻¹
 385 difference between our most upstream and downstream flux gates at Filchner-Ronne. Some small basins with little grounding



386 line discharge have very large proportional differences between estimates. For example, our discharge into Conger Glenzer
387 Ice Shelf is 1 Gt yr^{-1} or less than half of that in Rignot et al. (2019). In these cases, the absolute differences are comparable to
388 the error in the estimate and may due to the resolution of the flux gate used, as well as the choice of bed topography and ice
389 surface dataset.

390 **4.2 Implications for mass budget estimates**

391 At present, only one input-output estimate of Antarctic Ice Sheet mass balance is available (Rignot et al., 2019). This sparsity
392 of input-output data limits the otherwise comprehensive scope of ice sheet mass balance inter-comparison exercises (Otosaka
393 et al., 2023) and limits insights conferred by mass budget partitioning attempts. By providing discharge estimates derived using
394 a range of bed topography datasets, we hope that the community will take advantage of the full range of available SMB datasets
395 to compute Antarctic Ice Sheet mass change for any basin of interest, so as to enable deeper investigations into uncertainties
396 and drivers of Antarctic Ice Sheet mass change.

397 There is currently significant uncertainty in mass change estimates of some basins as calculated using the input-output method.
398 In some basins, the differences between available discharge estimates can lead to opposing conclusions regarding the overall
399 mass change of the basin. For example, Hansen et al. (2021) found opposing mass change trends on the Antarctic Peninsula
400 when using two different discharge datasets and a single SMB dataset. The mass change sensitivity to the choice of discharge
401 dataset will be particularly severe in basins from which the grounding line discharge is consistently above or below the
402 integrated SMB by an amount comparable to the error in the discharge estimates.

403 Whilst we think that our grounding line discharge estimate is the best that can currently be achieved using existing ice velocity,
404 ice thickness and firn air content estimates, we do not expect it to entirely resolve these challenges. We still find substantial
405 differences between (i) our primary discharge estimates from FrankenBed compared to those provided by FrankenBedAdj
406 (which we tuned to match independent mass loss observations) and (ii) the discharge estimates provided by Rignot et al.
407 (2019), who manually selected different approaches to determine grounding line discharge and who modified ice thickness in
408 a non-algorithmic manner in order to produce the required ice flux. In general, our FrankenBed discharge is lower than from
409 FrankenBedAdj and lower than in Rignot et al. (2019), implying less mass loss. There are only three plausible explanations
410 for these deviations. (1) The ice thickness used here is an underestimate of the true ice thickness in places where our ice flux
411 is too low, thereby leading us to underestimate grounding line discharge. (2) Basin-scale surface mass balance provided by the
412 mean of RACMO2.3p2, MAR and HIRHAM are too high, leading input-output mass balance to underestimate mass balance
413 even where the grounding line discharge is correct. (3) The mass loss estimates from gravimetric and altimetric approaches
414 are too great, possibly because of uncertainties in rates of glacial isostatic adjustment, which gravimetric approaches are
415 sensitive to, or uncertainties in the density of snow and ice contributing to the observed changes in surface elevation. Given
416 that Antarctic Ice Sheet mass changes estimated from gravimetry and altimetry agree much more closely with each other than
417 either do with the single available input-output mass change estimate (Otosaka et al., 2023), it seems unlikely that (3) is the



418 dominant contributor to the challenges facing the input-output method. If (1) were the sole contributor, then our thickness
419 adjustments in FrankenBedAdj provide a rough indication of the magnitude and location of poorly-constrained thickness in
420 existing bed products and could be used to guide future bed topographic mapping efforts. Given that the magnitude of the
421 thickness adjustments in FrankenBedAdj exceed 50 % in some places, and that these are typically in locations where SMB
422 and firn air content estimates from different regional climate models disagree the most, we think that factors (1) and (2) likely
423 contribute to the differences between mass budget approaches. It is our hope that synergistic use of each mass budget approach,
424 with due consideration for the location-specific uncertainties in each method, will lead to increased confidence regarding the
425 direction and magnitude of mass change around Antarctica, as well as improved understanding of the drivers of that mass
426 change.

427 **5 Data availability**

428 The ice sheet basins, balance discharge and grounding line discharge estimates are, for the purposes of review, available at:
429 <https://zenodo.org/records/10183327> (Davison et al., 2023a).

430 **6 Conclusions**

431 We present a new grounding line discharge product for Antarctica and all of its drainage basins available from 1996 through
432 to last month. The temporal resolution and coverage increases from annual and <25 % respectively in the early years of our
433 dataset to monthly and over 50 % respectively in the latter years of our dataset. We show that grounding line discharge from
434 Antarctica increased from $1,990 \pm 23 \text{ Gt yr}^{-1}$ in 1996, rising to $2,205 \pm 18 \text{ Gt yr}^{-1}$ in September 2023, with slight fluctuations
435 superimposed on this longer term increase. Much of this grounding line discharge change is due to increasing flow speeds of
436 West Antarctic ice streams, but we also observe large increases in discharge at some basins in East Antarctica, including Totten
437 Glacier, Vanderford Glacier, Denman Scott and Cook Ice Shelf. The high spatial resolution of our ice velocity mosaics since
438 October 2014 allow us to measure substantial seasonal variability and pronounced multi-year trends in discharge even on small
439 ~1 km-wide glaciers draining the Antarctic Peninsula.

440 There are substantial differences between our results and previous estimates during their overlapping time periods (Depoorter
441 et al., 2013; Gardner et al., 2018; Rignot et al., 2019). These differences generally arise due to uncertainties in bed topography,
442 which can accumulate across long flux gates or which represent a substantial proportion of the discharge across very short flux
443 gates, and due to differences in ice velocity resolution and flux gate position. For some basins, the differences between existing
444 discharge datasets, including our own, is significant enough to have bearing on the mass change of those basins when using
445 the input-output method, particularly in basins which remain close to balance but which are persistently above or below
446 balance. This is particularly acute on the Antarctic Peninsula and in parts of East Antarctica, where deriving estimates of ice



447 thickness, ice velocity, firn air content and surface mass balance are fraught with difficulties owing to the steep topography,
448 narrow glaciers, high snowfall and (in places) intense summertime surface melting.

449 We find that bed topography remains a potentially large uncertainty in grounding line discharge estimates and therefore has
450 the potential to severely limit the utility of attempts to calculate basin-scale ice mass change using the input-output method. In
451 order to reproduce observed rates of mass loss, we have to modify the bed topography by over 50 % in some basins. This may
452 be realistic in some places where the bed is poorly surveyed; however, uncertainties in SMB and uncertainties in independent
453 estimates of mass change will also contribute. The progressive increase in ice thickness measurements around Antarctica
454 (Frémand et al., 2023) and the improvements in assimilation and interpolation methods (Ji Leong and Joseph Horgan, 2020;
455 Morlighem et al., 2020) will lead to improved estimates of ice thickness around Antarctica – our workflow is designed to
456 facilitate the addition of new bed topography datasets as they become available and we aim to do so. We have provided this
457 dataset for the scientific community so as to ensure that accurate measurements of Antarctic grounding line discharge remain
458 available routinely for researchers everywhere.

459 **Appendix A: Making FrankenBedAdj bed topography**

460 Here we describe the method used to adjust the FrankenBed elevations such that the corresponding discharge estimate produces
461 the observed change in ice surface elevation.

462 The mass balance, M , of an ice sheet or ice sheet basin is given by:

$$463 \quad M = S - D, \quad (\text{A1})$$

464 where S is the surface mass balance and D is the grounding line discharge. For each of the MEaSUREs glacier basins, we
465 estimate the 1996 to 2014 average mass balance by integrating ice equivalent surface elevation change measurements over
466 each basin (Shepherd et al., 2019). The rates of elevation change from 1992 to 2023 are shown in Fig. A1. Using this rate of
467 mass change, we estimate the average discharge required to produce that mass change (Fig. A2), given the surface mass balance
468 anomalies from three regional climate models including RACMO2.3p2, MAR and HIRHAM5. We refer to this as our
469 altimetry-derived discharge.

470 For each basin, we proportionally adjust the pixel-based ice thickness based on the difference between our calculated basin-
471 scale discharge and the altimetry-derived discharge. This is akin to rearranging Eq. (4) to:

$$472 \quad H = D/Vw\rho, \quad (\text{A2})$$

473 Where V is the 1996 to 2014 average velocity normal to the flux gate in each pixel and D is the altimetry-derived discharge.
474 In w is the total length of the gate in each basin. In practice, this is an iterative process because we modify the pixel-based ice
475 thickness to solve for the basin-scale altimetry-derived discharge. The effect of these thickness adjustments are shown in Fig.
476 2 of the main text and Fig. A2.

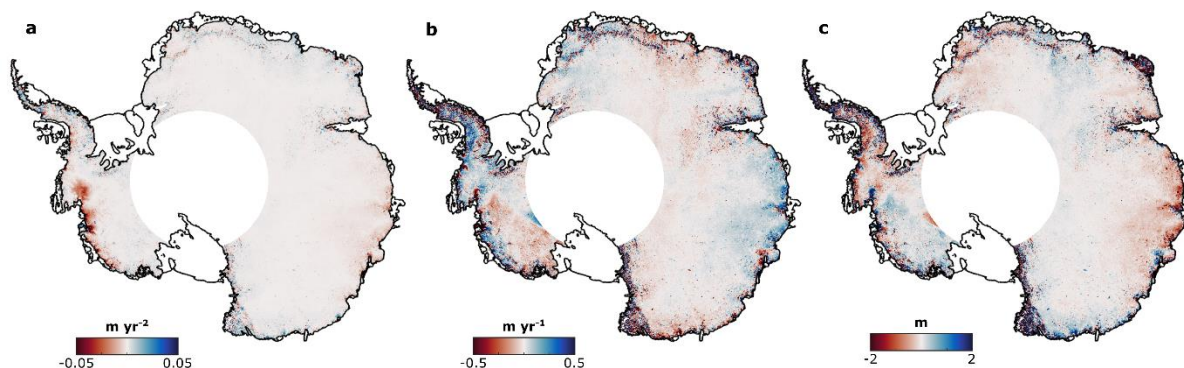


Figure A1. Coefficients from a time-dependent quadratic polynomial fitted to surface elevation change observations. The (a) acceleration, (b) linear and (c) intercept coefficients of the quadratic fit to observed surface elevation changes from 1992 to 2023 as measured by a suite of radar altimetry satellite missions.

477 This approach forces our 1996 to 2014 mean discharge derived from FrankenBedAdj to match the 1996 to 2014 mean discharge
478 inferred from ice sheet surface elevation change measurements and regional climate model output. As such, the
479 FrankenBedAdj discharge dataset is not fully independent of one altimetry-derived mass change estimate; therefore, we
480 recommend caution if using that subset of the dataset in inter-comparison exercises such as IMBIE. The FrankenBedAdj
481 estimate does, however, provide an indicator of which regions of existing Antarctic bed topography datasets may be under- or
482 over-estimating the bed elevation on average, especially in drainage basins where there is confidence in the velocity
483 measurements and SMB products. Given that our adjustment is a simple proportional shift of the FrankenBed profile across
484 each of the MEaSURES glacier basins, we do not intend FrankenBedAdj to be taken as a superior bed elevation product for
485 Antarctica. Our approach will be somewhat sensitive to the choice of basins used to perform the integration and it produces
486 unrealistic steps in bed elevation at the boundaries between basins. These steps have little impact on our grounding line
487 discharge estimate, but could be consequential if the modified bed data were used in, for example, ice sheet modelling
488 applications.

489

490

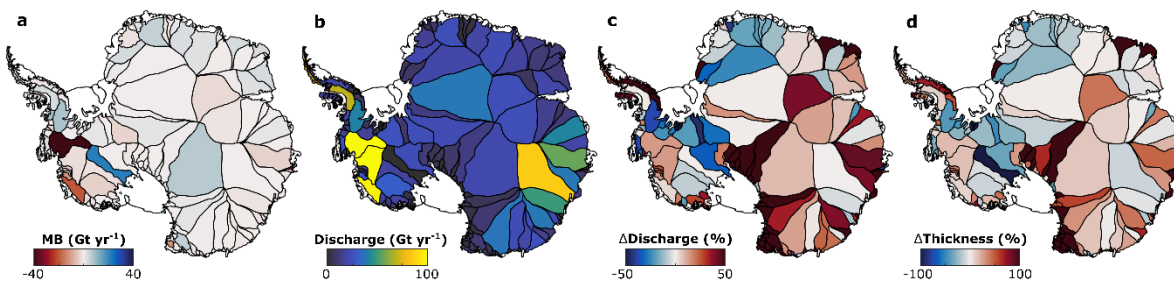


Figure A2. Creating FrankenBedAdj. (a) Observed rate of mass change from 1996 to 2014 based on the observed rates of ice surface elevation change in Figure A1. (b) Grounding line discharge, within each MEASUREs glacier basin, implied by the observed rates of mass change, given the surface mass balance from the mean of three regional climate models. (c) The percentage difference between the discharge in panel (b) and our average 1996-2014 discharge derived from FrankenBed. (d) The change in FrankenBed thickness required at the most downstream flux gate in order to reproduce panel (b).

491

492 Appendix B: Sentinel-1 ice velocity maps

493 We generate monthly velocity mosaics from October 2014 through to last month by applying standard intensity tracking
494 techniques (Strozzi et al., 2002) to Copernicus Sentinel-1 synthetic aperture radar (SAR) single look complex (SLC)
495 interferometric wide mode (IW) image pairs (Davison et al., 2023c; Hogg et al., 2017). We process all available 6- and 12-day
496 image pairs acquired over Antarctica; all image pairs prior to the launch of Sentinel-1b in April 2016 and after the failure of
497 Sentinel-1b in December 2021 are 12-day pairs. We estimate ice motion by performing a normalized cross-correlation between
498 image patches with dimensions 256 pixels in range and 64 pixels in azimuth, and a step size of 64 pixels in range and 16 pixels
499 in azimuth. To maximise tracking results in regions where velocity varies by more than an order of magnitude, we also use
500 patch sizes of 362x144 and 400x160 pixels over East and West Antarctica, and four further patch sizes on the Antarctic
501 Peninsula (192x48, 224x56, 288x72 and 320x80 pixels in range and azimuth). For scenes in East and West Antarctica, we use
502 the a 1 km DEM (Bamber et al., 2009), whereas for scenes in the Antarctic Peninsula we use the REMA 200 m DEM (Howat
503 et al., 2019). Prior to image cross-correlation, we perform image geocoding using the precise orbit ephemeris (accurate to 5
504 cm) where available and the restituted orbits otherwise (accurate to 10 cm) (Fernández et al., 2015). In common with
505 comparable estimates of Greenland Ice Sheet velocity (Solgaard et al., 2021), we find no significant difference between pairs
506 processed using each orbit type. Each image pair velocity field is posted on a 100x100 m grid in Antarctic Polar Stereographic
507 coordinates (EPSG 3031).



508 For each image pair, we generate a signal-to-noise ratio-weighted mean velocity field of all available cross-correlation window
509 sizes after removing outliers in the 2-D velocity fields. To remove outliers in each window size for every scene pair, we first
510 compare each speed field to a reference speed map (Rignot et al., 2017); speed estimates more than four times greater or four
511 times smaller than the reference map are considered outliers and removed. Secondly, flow directions more than 45 degrees
512 different from the reference map are considered outliers and removed. Thirdly, pixels in which the speed differs by more than
513 three standard deviations from its neighbours in a 5x5 moving window are removed. Similarly, pixels in which the flow
514 direction differs by more than 45 degrees from its neighbours in a 5x5 moving window are removed. Finally, we use a hybrid
515 median filter with a 3x3 moving window, which removes the central pixel if it more than three times the median of the
516 horizontally and diagonally connected pixels. After forming the signal-to-noise-ratio (SNR) weighted mean of the resulting
517 velocity fields, we generate Antarctic-wide mosaics of ice velocity for every unique date-pair since October 2014. From these
518 date-pair mosaics, we generate monthly Antarctic wide velocity mosaics as the mean of all date-pairs that overlap with the
519 target month. When doing so, we weight each date-pair by the number of days of overlap with the target month – in this way,
520 12-day pairs are weighted twice as much as 6-day pairs, which is appropriate because they should contribute more to the
521 average velocity in the month. We also generate two quality parameters, the number of observations in each month in each
522 pixel (after outlier removal) and the proportion of each month that is observed in each pixel, in addition to an error estimate
523 defined the speed divided by the SNR (Lemos et al., 2018).

524 **Author contribution**

525 BJD designed the study, generated the Sentinel-1 velocity data, designed and implemented the discharge algorithm, wrote the
526 manuscript and prepared all the figures. AEH acquired the funding and supported the Sentinel-1 velocity derivation. TS
527 contributed the ice surface elevation change observations. RR provided technical support on all aspects of the Sentinel-1
528 velocity derivation. All authors commented on the paper.

529 **Competing interests**

530 The authors declare that they have no competing interests.

531 **Acknowledgements**

532 This work was undertaken on ARC4 and ARC3, part of the High Performance Computing facilities at the University of Leeds,
533 UK. BJD gratefully acknowledges the European Space Agency and European Commission for providing Copernicus Sentinel-
534 1 data, as well as all the research teams who generated the ice thickness, ice velocity, surface mass balance, firn air content
535 and surface elevation change data that was used in this study, without which this research would not be possible.



536 **Financial support**

537 BJD and AEH are funded by: ESA via the ESA Polar+ Ice Shelves project (ESA-IPL-POE-EF-cb-LE-2019-834) and the SO-
538 ICE project (ESA AO/1-10461/20/I-NB); NERC via the DeCAdeS project (NE/T012757/1); and by the UK EO Climate
539 Information Service (NE/X019071/1).

540 **References**

541 Agosta, C., Amory, C., Kittel, C., Orsi, A., Favier, V., Gallée, H., Van Den Broeke, M. R., Lenaerts, J. T. M., Van Wessem,
542 J. M., Van De Berg, W. J. and Fettweis, X.: Estimation of the Antarctic surface mass balance using the regional climate model
543 MAR (1979-2015) and identification of dominant processes, *Cryosphere*, 13(1), 281–296, doi:10.5194/tc-13-281-2019, 2019.

544 Bamber, J., Gomez-Dans, J. L. and Griggs, J. A.: Antarctic 1 km Digital Elevation Model (DEM) from Combined ERS-1
545 Radar and ICESat Laser Satellite Altimetry, Version 1 [Data Set]., Boulder, Color. USA. NASA Natl. Snow Ice Data Cent.
546 Distrib. Act. Arch. Center., doi:10.5067/H0FQ1KL9NEKM, 2009.

547 Boxall, K., Christie, F. D. W., Willis, I. C., Wuite, J. and Nagler, T.: Seasonal land-ice-flow variability in the Antarctic
548 Peninsula, *Cryosphere*, 16(10), 3907–3932, doi:10.5194/tc-16-3907-2022, 2022.

549 Cook, A. J., Vaughan, D. G., Luckman, A. J. and Murray, T.: A new Antarctic Peninsula glacier basin inventory and observed
550 area changes since the 1940s, *Antarct. Sci.*, 26(6), 614–624, doi:10.1017/S0954102014000200, 2014.

551 Cui, X., Jeofry, H., Greenbaum, J. S., Guo, J., Li, L., Lindzey, L. E., Habbal, F. A., Wei, W., Young, D. A., Ross, N.,
552 Morlighem, M., Jong, L. M., Roberts, J. L., Blankenship, D. D., Bo, S. and Siegert, M. J.: Bed topography of Princess Elizabeth
553 Land in East Antarctica, *Earth Syst. Sci. Data*, 12(4), 2765–2774, doi:10.5194/essd-12-2765-2020, 2020.

554 Davison, B., Hogg, A., Slater, T. and Rigby, R.: Antarctic Ice Sheet grounding line discharge from 1996 to through 2023 [Data
555 set], Zenodo, doi:<https://zenodo.org/records/10128573>, 2023a.

556 Davison, B. J., Hogg, A. E., Gourmelen, N., Jakob, L., Wuite, J., Nagler, T., Greene, C. A., Andreasen, J. and Engdahl, M. E.:
557 Annual mass budget of Antarctic ice shelves from 1997 to 2021, *Sci. Adv.*, 2023b.

558 Davison, B. J., Hogg, A. E., Rigby, R., Veldhuijsen, S., van Wessem, J. M., van den Broeke, M. R., Holland, P. R., Selley, H.
559 L. and Dutrieux, P.: Sea level rise from West Antarctic mass loss significantly modified by large snowfall anomalies, *Nat.*
560 *Commun.*, 14(1), doi:10.1038/s41467-023-36990-3, 2023c.

561 Depoorter, M. A., Bamber, J. L., Griggs, J. A., Lenaerts, J. T. M., Ligtenberg, S. R. M., Van Den Broeke, M. R. and Moholdt,



- 562 G.: Calving fluxes and basal melt rates of Antarctic ice shelves, *Nature*, 502(7469), 89–92, doi:10.1038/nature12567, 2013.
- 563 Diener, T., Sasgen, I., Agosta, C., Fürst, J. J., Braun, M. H., Konrad, H. and Fettweis, X.: Acceleration of Dynamic Ice Loss
564 in Antarctica From Satellite Gravimetry, *Front. Earth Sci.*, 9(December), 1–17, doi:10.3389/feart.2021.741789, 2021.
- 565 Fernández, J., Escobar, D., Bock, H. and Féménias, P.: Copernicus POD Operations - Orbital Accuracy of Sentinel-1A and
566 Sentinel-2A, 25th Int. Symp. Sp. Flight Dyn. 4.2. An optional note, 201–213, 2015.
- 567 Frémand, A. C., Fretwell, P., Bodart, J. A., Pritchard, H. D., Aitken, A., Bamber, J. L., Bell, R. E., Bianchi, C., Bingham, R.
568 G., Blankenship, D. D., Casassa, G., Catania, G. A., Christianson, K., Conway, H., Corr, H. F. J., Cui, X., Damaske, D., Damm,
569 V., Drews, R., Eagles, G., Eisen, O., Eisermann, H., Ferraccioli, F., Field, E., Forsberg, R., Franke, S., Fujita, S., Gim, Y.,
570 Goel, V., Gogineni, S. ., Greenbaum, J. S., Hills, B., Hindmarsh, R. C. A., Hoffman, A. O., Holmlund, P., Holschuh, N., Holt,
571 J. W., Horlings, A., Humbert, A., Jacobel, R. W., Daniela, J., Jenkins, A., Jokat, W., Jordan, T., King, E., Kohler, J., Krabill,
572 W., Gillespie, M., Langley, K., Lee, J., Leitchenkov, G., Leuschen, C., Luyendyk, B., MacGregor, J. A., MacKie, E., Matsuoka,
573 K., Morlighem, M., Mouginot, J., Nitsche, F. ., Nogi, Y., Nost, O. A., Paden, J. D., Pattyn, F., Popov, S. V., Rignot, E., Rippin,
574 D. M., Rivera, A., Roberts, J., Ross, N., Rupper, A., Schroeder, D. M., Siegert, M. J., Smith, A. M., Steinhage, D., Studinger,
575 M., Sun, B., Tabacco, I., Tinto, K. J., Stefano, U., Vaughan, D. G., Welch, B. C., Wilson, D., Young, D. A. and Zirizzotti, A.:
576 Antarctic Bedmap data: Findable, Accessible, Interoperable, and Reusable (FAIR) sharing of 60 years of ice bed, surface, and
577 thickness data, *Earth Syst. Sci. Data*, 15, 2695–2710, doi:10.5194/essd-15-2695-2023, 2023.
- 578 Fretwell, P., Pritchard, H. D., Vaughan, D. G., Bamber, J. L., Barrand, N. E., Bell, R., Bianchi, C., Bingham, R. G.,
579 Blankenship, D. D., Casassa, G., Catania, G., Callens, D., Conway, H., Cook, A. J., Corr, H. F. J., Damaske, D., Damm, V.,
580 Ferraccioli, F., Forsberg, R., Fujita, S., Gim, Y., Gogineni, P., Griggs, J. A., Hindmarsh, R. C. A., Holmlund, P., Holt, J. W.,
581 Jacobel, R. W., Jenkins, A., Jokat, W., Jordan, T., King, E. C., Kohler, J., Krabill, W., Riger-Kusk, M., Langley, K. A.,
582 Leitchenkov, G., Leuschen, C., Luyendyk, B. P., Matsuoka, K., Mouginot, J., Nitsche, F. O., Nogi, Y., Nost, O. A., Popov, S.
583 V., Rignot, E., Rippin, D. M., Rivera, A., Roberts, J., Ross, N., Siegert, M. J., Smith, A. M., Steinhage, D., Studinger, M., Sun,
584 B., Tinto, B. K., Welch, B. C., Wilson, D., Young, D. A., Xiangbin, C. and Zirizzotti, A.: Bedmap2: Improved ice bed, surface
585 and thickness datasets for Antarctica, *Cryosphere*, 7(1), 375–393, doi:10.5194/tc-7-375-2013, 2013.
- 586 Gardner, A.: Spatially and temporally continuous reconstruction of Antarctic Amundsen Sea sector ice sheet surface velocities:
587 1996-2018 [Data set], Zenodo, doi:10.5281/zenodo.7809354, 2023.
- 588 Gardner, A. S., Moholdt, G., Scambos, T., Fahnestock, M., Ligtenberg, S., Van Den Broeke, M. and Nilsson, J.: Increased West
589 Antarctic and unchanged East Antarctic ice discharge over the last 7 years, *Cryosphere*, 12(2), 521–547, doi:10.5194/tc-12-
590 521-2018, 2018.



- 591 Gardner, A. S., Fahnestock, M. A. and Scambos, T. A.: ITS_LIVE Regional Glacier and Ice Sheet Surface Velocities (National
592 Snow and Ice Data Center, 2019); <https://doi.org/10.5067/6II6VW8LLWJ7>, 2019.
- 593 Greene, C., Gardner, A. S., Schlegel, N.-J. and Fraser, A. D.: Antarctic calving loss rivals ice shelf thinning, *Nature*,
594 30(January), doi:10.1038/s41586-022-05037-w, 2022.
- 595 Greene, C. A., Thirumalai, K., Kearney, K. A., Delgado, J. M., Schwanghart, W., Wolfenbarger, N. S., Thyng, K. M., Gwyther,
596 D. E., Gardner, A. S. and Blankenship, D. D.: The Climate Data Toolbox for MATLAB, *Geochemistry, Geophys. Geosystems*,
597 20(7), 3774–3781, doi:10.1029/2019GC008392, 2019.
- 598 Hansen, N., Langen, P. L., Boberg, F., Forsberg, R., Simonsen, S. B., Thejll, P., Vandecrux, B. and Mottram, R.: Downscaled
599 surface mass balance in Antarctica: Impacts of subsurface processes and large-scale atmospheric circulation, *Cryosphere*,
600 15(9), 4315–4333, doi:10.5194/tc-15-4315-2021, 2021.
- 601 Haran, T., Klinger, M., Bohlander, J., Fahnestock, M., Painter, T. and Scambos, T.: MEaSURES MODIS Mosaic of Antarctica
602 2013-2014 (MOA2014) Image Map, Version 1, Boulder, Color. USA. NASA Natl. Snow Ice Data Cent. Distrib. Act. Arch.
603 Center., doi:<https://doi.org/10.5067/RNF17BP824UM>, 2018.
- 604 Hogg, A. E., Shepherd, A., Cornford, S. L., Briggs, K. H., Gourmelen, N., Graham, J. A., Joughin, I., Mouginot, J., Nagler,
605 T., Payne, A. J., Rignot, E. and Wuite, J.: Increased ice flow in Western Palmer Land linked to ocean melting, *Geophys. Res.*
606 *Lett.*, 44(9), 4159–4167, doi:10.1002/2016GL072110, 2017.
- 607 Howat, I. M., Porter, C., Smith, B. E., Noh, M. J. and Morin, P.: The reference elevation model of antarctica, *Cryosphere*,
608 13(2), 665–674, doi:10.5194/tc-13-665-2019, 2019.
- 609 Huss, M. and Farinotti, D.: A high-resolution bedrock map for the Antarctic Peninsula, *Cryosphere*, 8(4), 1261–1273,
610 doi:10.5194/tc-8-1261-2014, 2014.
- 611 Ji Leong, W. and Joseph Horgan, H.: DeepBedMap: A deep neural network for resolving the bed topography of Antarctica,
612 *Cryosphere*, 14(11), 3687–3705, doi:10.5194/tc-14-3687-2020, 2020.
- 613 Joughin, I., Shapero, D., Smith, B., Dutrioux, P. and Barham, M.: Ice-shelf retreat drives recent Pine Island Glacier speedup,
614 *Sci. Adv.*, 7(24), 1–7, doi:10.1126/sciadv.abg3080, 2021.
- 615 Kittel, C., Amory, C., Agosta, C., Delhasse, A., Doutreloup, S., Huot, P. V., Wyard, C., Fichet, T. and Fettweis, X.:
616 Sensitivity of the current Antarctic surface mass balance to sea surface conditions using MAR, *Cryosphere*, 12(12), 3827–
617 3839, doi:10.5194/tc-12-3827-2018, 2018.



- 618 Konrad, H., Gilbert, L., Cornford, S. L., Payne, A., Hogg, A. E., Muir, A. and Shepherd, A.: Uneven onset and pace of ice-
619 dynamical imbalance in the Amundsen Sea, *Geophys. Res. Lett.*, 44, 910–918, doi:10.1002/2016GL070733, 2017.
- 620 Lemos, A., Shepherd, A., Mcmillan, M., Hogg, A. E., Hatton, E. and Joughin, I.: Ice velocity of Jakobshavn Isbræ , Petermann
621 Glacier , Nioghalvfjærdssjø rden and Zachariæ Isstrøm , 2015-2017 , from Sentinel 1-a / b SAR imagery, *Cryosph. Discuss.*,
622 (February) [online] Available from: <https://doi.org/10.5194/tc-2017-251>, 2018.
- 623 Mankoff, K. D., Colgan, W., Solgaard, A., Karlsson, N. B., Ahlstrøm, A. P., van As, D., Box, J. E., Abbas Khan, S., Kjeldsen,
624 K. K., Mouginot, J. and Fausto, R. S.: Greenland Ice Sheet solid ice discharge from 1986 through 2017, *Earth Syst. Sci. Data*,
625 11, 769–786, doi:10.5194/essd-11-769-2019, 2019.
- 626 Mankoff, K. D., Solgaard, A., Colgan, W., Ahlstrøm, A. P., Abbas Khan, S. and Fausto, R. S.: Greenland Ice Sheet solid ice
627 discharge from 1986 through March 2020, *Earth Syst. Sci. Data*, 12(2), 1367–1383, doi:10.5194/essd-12-1367-2020, 2020.
- 628 Medley, B., Neumann, T., Zwally, H. J., Smith, B. E. and Stevens, C. M.: NASA GSFC Firn Densification Model version
629 1.2.1 (GSFC-FDMv1.2.1) for the Greenland and Antarctic Ice Sheets: 1980-2022 (1.2.1 release 2) [Data set], Zenodo,
630 doi:10.5281/zenodo.7221954, 2022a.
- 631 Medley, B., Neumann, T. A., Zwally, H. J., Smith, B. E. and Stevens, C. M.: Simulations of firn processes over the Greenland
632 and Antarctic ice sheets: 1980-2021, *Cryosphere*, 16(10), 3971–4011, doi:10.5194/tc-16-3971-2022, 2022b.
- 633 Miles, B. W. J., Stokes, C. R., Jamieson, S. S. R., Jordan, J. R., Gudmundsson, G. H. and Jenkins, A.: High spatial and temporal
634 variability in Antarctic ice discharge linked to ice shelf buttressing and bed geometry, *Sci. Rep.*, 1–14, doi:10.1038/s41598-
635 022-13517-2, 2022.
- 636 Morlighem, M.: MEaSURES BedMachine Antarctica, Version 2, Boulder, Color. USA. NASA Natl. Snow Ice Data Cent.
637 Distrib. Act. Arch. Cent., doi:10.5067/E1QL9HFQ7A8M, 2020.
- 638 Morlighem, M., Rignot, E., Binder, T., Blankenship, D., Drews, R., Eagles, G., Eisen, O., Ferraccioli, F., Forsberg, R.,
639 Fretwell, P., Goel, V., Greenbaum, J. S., Gudmundsson, H., Guo, J., Helm, V., Hofstede, C., Howat, I., Humbert, A., Jokat,
640 W., Karlsson, N. B., Lee, W. S., Matsuoka, K., Millan, R., Mouginot, J., Paden, J., Pattyn, F., Roberts, J., Rosier, S., Ruppel,
641 A., Seroussi, H., Smith, E. C., Steinhage, D., Sun, B., Broeke, M. R. van den, Ommen, T. D. van, Wessem, M. van and Young,
642 D. A.: Deep glacial troughs and stabilizing ridges unveiled beneath the margins of the Antarctic ice sheet, *Nat. Geosci.*, 13(2),
643 132–137, doi:10.1038/s41561-019-0510-8, 2020.
- 644 Mottram, R., Hansen, N., Kittel, C., Van Wessem, J. M., Agosta, C., Amory, C., Boberg, F., Van De Berg, W. J., Fettweis, X.,



- 645 Gossart, A., Van Lipzig, N. P. M., Van Meijgaard, E., Orr, A., Phillips, T., Webster, S., Simonsen, S. B. and Souverijns, N.:
646 What is the surface mass balance of Antarctica? An intercomparison of regional climate model estimates., 2021.
- 647 Mouginit, J., Rignot, E. and Scheuchl, B.: Sustained increase in ice discharge from the Amundsen Sea Embayment, West
648 Antarctica, from 1973 to 2013, *Geophys. Res. Lett.*, 41(5), 1576–1584, doi:10.1002/2013GL059069, 2014.
- 649 Mouginit, J., Rignot, E., Scheuchl, B. and Millan, R.: Comprehensive annual ice sheet velocity mapping using Landsat-8,
650 Sentinel-1, and RADARSAT-2 data, *Remote Sens.*, 9(4), 1–20, doi:10.3390/rs9040364, 2017a.
- 651 Mouginit, J., Scheuchl, B. and Rignot, E.: MEaSUREs Annual Antarctic Ice Velocity Maps, Version 1, Boulder, Color. USA.
652 NASA Natl. Snow Ice Data Cent. Distrib. Act. Arch. Cent., doi:10.5067/9T4EPQXTJYW9, 2017b.
- 653 Mouginit, J., Scheuchl, B. and Rignot, E.: MEaSUREs Antarctic Boundaries for IPY 2007-2009 from Satellite Radar, Version
654 2, Boulder, Color. USA. NASA Natl. Snow Ice Data Cent. Distrib. Act. Arch. Cent., doi:10.5067/AXE4121732AD, 2017c.
- 655 Ootaka, I. N., Shepherd, A., Ivins, E. R., Schlegel, N. J., Amory, C., Van Den Broeke, M. R., Horwath, M., Joughin, I., King,
656 M. D., Krinner, G., Nowicki, S., Payne, A. J., Rignot, E., Scambos, T., Simon, K. M., Smith, B. E., Sørensen, L. S., Velicogna,
657 I., Whitehouse, P. L., Geruo, A., Agosta, C., Ahlstrøm, A. P., Blazquez, A., Colgan, W., Engdahl, M. E., Fettweis, X., Forsberg,
658 R., Gallée, H., Gardner, A., Gilbert, L., Gourmelen, N., Groh, A., Gunter, B. C., Harig, C., Helm, V., Khan, S. A., Kittel, C.,
659 Konrad, H., Langen, P. L., Lecavalier, B. S., Liang, C. C., Loomis, B. D., McMillan, M., Melini, D., Mernild, S. H., Mottram,
660 R., Mouginit, J., Nilsson, J., Noël, B., Pattle, M. E., Peltier, W. R., Pie, N., Roca, M., Sasgen, I., Save, H. V., Seo, K. W.,
661 Scheuchl, B., Schrama, E. J. O., Schröder, L., Simonsen, S. B., Slater, T., Spada, G., Sutterley, T. C., Vishwakarma, B. D.,
662 Van Wessem, J. M., Wiese, D., Van Der Wal, W. and Wouters, B.: Mass balance of the Greenland and Antarctic ice sheets
663 from 1992 to 2020, *Earth Syst. Sci. Data*, 15(4), 1597–1616, doi:10.5194/essd-15-1597-2023, 2023.
- 664 Paolo, F., Gardner, A., Greene, C., Nilsson, J., Schodlok, M., Schlegel, N. and Fricker, H.: Widespread slowdown in thinning
665 rates of West Antarctic Ice Shelves, *Cryosph.*, 17, 3409–3433, doi:10.5194/tc-17-3409-2023, 2023.
- 666 Rignot, E., Mouginit, J. and Scheuchl, B.: MEaSUREs InSAR-Based Ice Velocity of the Amundsen Sea Embayment,
667 Antarctica, Version 1, Boulder, Color. USA. NASA Natl. Snow Ice Data Cent. Distrib. Act. Arch. Cent.,
668 doi:<https://doi.org/10.5067/MEASURES/CRYOSPHERE/nsidc-0545.001>, 2014.
- 669 Rignot, E., Mouginit, J. and Scheuchl, B.: MEaSUREs InSAR-Based Antarctica Ice Velocity Map, Version 2, Boulder, Color.
670 USA. NASA Natl. Snow Ice Data Cent. Distrib. Act. Arch. Center., doi:<https://doi.org/10.5067/D7GK8F5J8M8R>, 2017.
- 671 Rignot, E., Mouginit, J., Scheuchl, B., Van Den Broeke, M., Van Wessem, M. J. and Morlighem, M.: Four decades of Antarctic



- 672 ice sheet mass balance from 1979–2017, *Proc. Natl. Acad. Sci. U. S. A.*, 116(4), 1095–1103, doi:10.1073/pnas.1812883116,
673 2019.
- 674 Rignot, E., Scheuchl, B. and Mouginot, J.: MEaSUREs Multi-year Reference Velocity Maps of the Antarctic Ice Sheet,
675 Version 1, Boulder, Color. USA. NASA Natl. Snow Ice Data Cent., doi:10.5067/FB851ZIZYX5O, 2022.
- 676 Selley, H. L., Hogg, A. E., Cornford, S., Dutrieux, P., Shepherd, A., Wuite, J., Floricioiu, D., Kusk, A., Nagler, T., Gilbert, L.,
677 Slater, T. and Kim, T.: Widespread increase in dynamic imbalance in the Getz region of Antarctica from 1994 to 2018, *Nat.*
678 *Commun.*, 12(1133), doi:10.1038/s41467-021-21321-1, 2021.
- 679 Shepherd, A., Ivins, E., Rignot, E., Smith, B., Van Den Broeke, M., Velicogna, I., Whitehouse, P., Briggs, K., Joughin, I.,
680 Krinner, G., Nowicki, S., Payne, T., Scambos, T., Schlegel, N., Geruo, A., Agosta, C., Ahlstrøm, A., Babonis, G., Barletta, V.,
681 Blazquez, A., Bonin, J., Csatho, B., Cullather, R., Felikson, D., Fettweis, X., Forsberg, R., Gallee, H., Gardner, A., Gilbert, L.,
682 Groh, A., Gunter, B., Hanna, E., Harig, C., Helm, V., Horvath, A., Horvath, M., Khan, S., Kjeldsen, K. K., Konrad, H.,
683 Langen, P., Lecavalier, B., Loomis, B., Luthcke, S., McMillan, M., Melini, D., Mernild, S., Mohajerani, Y., Moore, P.,
684 Mouginot, J., Moyano, G., Muir, A., Nagler, T., Nield, G., Nilsson, J., Noel, B., Ootosaka, I., Pattle, M. E., Peltier, W. R., Pie,
685 N., Rietbroek, R., Rott, H., Sandberg-Sørensen, L., Sasgen, I., Save, H., Scheuchl, B., Schrama, E., Schröder, L., Seo, K. W.,
686 Simonsen, S., Slater, T., Spada, G., Sutterley, T., Talpe, M., Tarasov, L., Van De Berg, W. J., Van Der Wal, W., Van Wessem,
687 M., Vishwakarma, B. D., Wiese, D. and Wouters, B.: Mass balance of the Antarctic Ice Sheet from 1992 to 2017, *Nature*, 558,
688 219–222, doi:10.1038/s41586-018-0179-y, 2018.
- 689 Shepherd, A., Gilbert, L., Muir, A. S., Konrad, H., McMillan, M., Slater, T., Briggs, K. H., Sundal, A. V., Hogg, A. E. and
690 Engdahl, M. E.: Trends in Antarctic Ice Sheet Elevation and Mass, *Geophys. Res. Lett.*, 46(14), 8174–8183,
691 doi:10.1029/2019GL082182, 2019.
- 692 Slater, T., Lawrence, I. R., Ootosaka, I. N., Shepherd, A., Gourmelen, N., Jakob, L., Tepes, P., Gilbert, L. and Nienow, P.:
693 Review article: Earth’s ice imbalance, *Cryosphere*, 15(1), 233–246, doi:10.5194/tc-15-233-2021, 2021.
- 694 Smith, B., Fricker, H. A., Gardner, A. S., Medley, B., Nilsson, J., Paolo, F. S., Holschuh, N., Adusumilli, S., Brunt, K., Csatho,
695 B., Harbeck, K., Markus, T., Neumann, T., Siegfried, M. R. and Zwally, H. J.: Pervasive ice sheet mass loss reflects competing
696 ocean and atmosphere processes, *Science* (80-.), 1242(6496), 1239–1242, doi:10.1126/science.aaz5845, 2020.
- 697 Solgaard, A., Kusk, A., Boncori, J. P. M., Dall, J., Mankoff, K. D., Ahlstrøm, A. P., Andersen, S. B., Citterio, M., Karlsson,
698 N. B., Kjeldsen, K. K., Korsgaard, N. J., Larsen, S. H. and Fausto, R. S.: Greenland ice velocity maps from the PROMICE
699 project, *Earth Syst. Sci. Data*, 13(7), 3491–3512, doi:10.5194/essd-13-3491-2021, 2021.



- 700 Strozzi, T., Luckman, A., Murray, T., Wegmuler, U. and Werner, C. L.: Glacier motion estimation using SAR offset-tracking
701 procedures, *IEEE Trans. Geosci. Remote Sens.*, 40, 2384–2391, doi:10.1109/TGRS.2002.805079, 2002.
- 702 Sutterley, T. C., Velicogna, I., Rignot, E., Mouginot, J., Flament, T., Van Den Broeke, M. R., Van Wessem, J. M. and Reijmer,
703 C. H.: Mass loss of the Amundsen Sea Embayment of West Antarctica from four independent techniques, *Geophys. Res. Lett.*,
704 41(23), 8421–8428, doi:10.1002/2014GL061940, 2014.
- 705 Sutterley, T. C., Velicogna, I. and Hsu, C.-W.: Self-Consistent Ice Mass Balance and Regional Sea Level From Time-Variable
706 Gravimetry, *Earth Sp. Sci.*, 7, e2019EA000860, doi:10.1029/2019EA000860, 2020.
- 707 Veldhuijsen, Sanne, B. M., van de Berg, W. J., Brils, M., Munneke, P. K. and van den Broeke, M. R.: Characteristics of the
708 contemporary Antarctic firm layer simulated with IMAU-FDM v1.2A (1979-2020), *Cryosph. Discuss.*, doi:10.5194/tc-2022-
709 118, 2022.
- 710 Velicogna, I., Mohajerani, Y., Geruo, A., Landerer, F., Mouginot, J., Noel, B., Rignot, E., Sutterley, T., van den Broeke, M.,
711 van Wessem, M. and Wiese, D.: Continuity of Ice Sheet Mass Loss in Greenland and Antarctica From the GRACE and GRACE
712 Follow-On Missions, *Geophys. Res. Lett.*, 47(8), 1–8, doi:10.1029/2020GL087291, 2020.
- 713 Wallis, B. J., Hogg, A. E., van Wessem, J. M., Davison, B. J. and van den Broeke, M. R.: Widespread seasonal speed-up of
714 west Antarctic Peninsula glaciers from 2014 to 2021, *Nat. Geosci.*, 16(3), 231–237, doi:10.1038/s41561-023-01131-4, 2023.
- 715 van Wessem, J. M., van de Berg, W. J., Noël, B. P. Y., van Meijgaard, E., Birnbaum, G., Jakobs, C. L., Krüger, K., Lenaerts,
716 J. T. M., Lhermitte, S., Ligtenberg, S. R. M., Medley, B., Reijmer, C. H., van Tricht, K., Trusel, L. D., van Ulf, L. H., Wouters,
717 B., Wuite, J. and van den Broeke, M. R.: Modelling the climate and surface mass balance of polar ice sheets using RACMO2,
718 part 2: Antarctica (1979-2016), *Cryosph.*, 12, 1479–1498, doi:10.5194/tc-12-1479-2018, 2018.
- 719 Zwally, H. J., Giovinetto, M. B., Beckley, M. A. and Saba, J. L.: Antarctic and Greenland Drainage Systems, GSFC
720 Cryospheric Sci. Lab., doi:http://icesat4.gsfc.nasa.gov/cryo_data/ant_grn_drainage_systems.php, 2012.

721

722